Sub-arcsecond [Fe ii] spectro-imaging of the DG Tauri jet. Periodic bubbles and a dusty disk wind?

V. Agra-Amboage, C. Dougados, S. Cabrit, J. Reunanen

Astronomy & Astrophysics

Sub-arcsecond [Fe II] spectro-imaging of the DG Tauri jet

Periodic bubbles and a dusty disk wind?

V. Agra-Amboage[1], C. Dougados[1], S. Cabrit[2], and J. Reunanen[3]

[1] UJF-Grenoble 1/CNRS-INSU, Institut de Planétologie et d'Astrophysique de Grenoble (IPAG) UMR 5274, 38041 Grenoble, France
e-mail: vaa@fe.up.pt; catherine.dougados@obs.ujf-grenoble.fr

[2] LERMA, Observatoire de Paris, UMR 8112 du CNRS, 61 avenue de l'Observatoire, 75014 Paris, France
e-mail: sylvie.cabrit@obspm.fr

[3] Tuorla Observatory, Department of Physics and Astronomy, University of Turku, Vaisalantie 20, 21500 Piikkio, Finland

ABSTRACT

Context. The origin of protostellar jets as well as their impact on the regulation of angular momentum and the inner disk physics are still crucial open questions in star formation.

Aims. We aim to test the different proposed ejection processes in T Tauri stars through high-angular resolution observations of forbidden-line emission from the inner DG Tauri microjet.

Methods. We present spectro-imaging observations of the DG Tauri jet obtained with SINFONI/VLT in the lines of [Fe II]$\lambda 1.64$ μm, 1.53 μm with $0\farcs15$ angular resolution and $R = 3000$ spectral resolution. We analyze the morphology and kinematics, derive electronic densities and mass-flux rates and discuss the implications for proposed jet launching models.

Results. (1) We observe an onion-like velocity structure in [Fe II] in the blueshifted jet, similar to that observed in optical lines. High-velocity (HV) gas at $\simeq -200$ km s^{-1} is collimated inside a half-opening angle of 4° and medium-velocity (MV) gas at $\simeq -100$ km s^{-1} in a cone with an half-opening angle $14°.$ (2) Two new axial jet knots are detected in the blue jet, as well as a more distant bubble with corresponding counter-bubble. The periodic knot ejection timescale is revised downward to 2.5 yrs. (3) The redshifted jet is detected only beyond $0\farcs7$ from the star, yielding revised constraints on the disk surface density. (4) From comparison to [O I] data we infer iron depletion of a factor 3 at high velocities and a factor 10 at speeds below -100 km s^{-1}. (5) The mass-fluxes in each of the medium and high-velocity components of the blueshifted lobe are $\simeq 1.6 \pm 0.8 \times 10^{-8}$ $M_\odot$ yr^{-1}, representing $0.02-0.2$ of the disk accretion rate.

Conclusions. The medium-velocity conical [Fe II] flow in the DG Tau jet is too fast and too narrow to trace photo-evaporated matter from the disk atmosphere. Both its kinematics and collimation cannot be reproduced by the X-wind, nor can the "conical magnetospheric wind". The level of Fe gas phase depletion in the DG Tau medium-velocity component also rules out a stellar wind and a cocoon ejected sideways from the high-velocity beam. A quasi-steady centrifugal MHD disk wind ejected over $0.25-1.5$ AU and/or episodic magnetic tower cavities launched from the disk appear as the most plausible origins for the [Fe II] medium velocity component in the DG Tau jet. The same disk wind model can also account for the properties of the high-velocity [Fe II] flow, although alternative origins in magnetospheric and/or stellar winds cannot be excluded for this component.

Key words. stars: pre-main sequence – stars: individual: DG Tau – ISM: jets and outflows – ISM: individual objects: HH158 – techniques: imaging spectroscopy – techniques: high angular resolution

1. Introduction

The physical mechanism by which mass is ejected from accreting young stars and is collimated into jets and the role that these jets play in solving the angular momentum problem of star formation remain fundamental open questions. It is now widely accepted that the action of magnetic fields is required to explain the efficient jet collimation and acceleration (Cabrit 2007a). However, several MHD ejection sites may operate in parallel: the stellar surface, reconnection points in the stellar magnetosphere, the inner disk edge or a broader range of disk radii, and their relative contribution to the jet remains subject to debate (see e.g. Ferreira et al. 2006; Edwards 2009, and references therein for a recent review).

Distinguishing between these scenarii is crucial not only for understanding the role of jets in star formation, but also for planetary formation and disk evolution. For example, the equipartition magnetic field required to launch a powerful MHD disk wind could affect planetary migration (Terquem 2003) and

would speed up the accretion flow inside the launch zone, lowering the disk surface density by several orders of magnitude compared to a standard viscous disk model (Combet & Ferreira 2008).

Strong observational constraints on the jet driving mechanism in young stars come from studies of extended forbidden line emission in "microjets" from young low-mass (≤ 2 $M_\odot$) T Tauri stars (TTS). Their proximity and lack of obscuring envelope give access to inner jet regions within $20-200$ AU where the flow structure has, hopefully, not yet been significantly perturbed by interaction with the ambient medium. In addition, the optically thin forbidden lines provide powerful tracers of jet density and excitation. In particular, a wealth of data on jet widths, kinematics, and density and ionization structure has been obtained over the last 10 years in the optical range, thanks to the sub-arcsecond resolution provided by adaptive optics on the ground and HST/STIS (see the review by Ray et al. 2007, and references therein). Confronting proposed ejection models with these data, Ferreira et al. (2006) proposed that centrifugal disk winds

appear the most promising to reproduce simultaneously all forbidden line jet observations, and that these disk winds could confine the hot inner stellar/magnetospheric winds inferred, e.g., from He I line profiles (Kwan et al. 2007).

Support for an extended MHD disk wind is most evident in the bright and well-studied jet HH 158 from the actively accreting T Tauri star DG Tauri (Mundt & Fried 1983). An onion-like structure is observed within 500 AU of the star in optical forbidden emission lines, with faster gas nested inside slower material (Lavalley-Fouquet et al. 2000; Bacciotti et al. 2000). This behavior is naturally expected if the wind is launched from a broad range of disk radii. Furthermore, the slowest jet material at $V_r \simeq 30-60$ km s^{-1} exhibits velocity shifts between the two sides of the jet (Bacciotti et al. 2000; Coffey et al. 2007) in the same sense as the rotation of the DG Tau disk (Testi et al. 2002). These transverse shifts excellently agree with predicted rotation signatures for a steady-state MHD disk wind launched out to about 3 AU (Anderson et al. 2003; Pesenti et al. 2004; Ferreira et al. 2006). A velocity shift in the same sense is seen across faster jet material at -200 km s^{-1} suggesting (if caused by rotation) ejection from smaller disk radii of $\simeq 0.2-0.5$ AU (Coffey et al. 2007).

However, rotation signatures alone are insufficient to firmly establish a disk wind origin for the DG Tau jet, because velocity shifts might be contaminated by other effects, such as jet precession or non-axisymmetric shocks (Cerqueira et al. 2006; Soker 2005). Alternative explanations for the broader, slow component in forbidden lines could be, e.g., a cocoon of gas ejected sideways from the central fast jet beam or ambient swept-up gas. To further test these alternatives, more information is needed such as the full flow morphology in 2D, accurate mass-fluxes, and dust content.

Another open question is whether the fast and slow material seen in forbidden lines in the DG Tauri jet share a similar origin or if they trace two distinct ejection sites and ejection mechanisms. A dual origin in a magnetospheric wind and a disk wind was proposed by Pyo et al. (2003) for the emission in [Fe II] from long-slit observations at high spectral resolution (30 km s^{-1}) based on the double-peaked profile with a high-velocity component at about -200 km s^{-1} and a low-velocity component at about -100 km s^{-1}, of relative strength varying along the jet. In contrast, a single disk wind where the ionization fraction varies continuously from inner to outer streamlines would predict a smooth single-peaked profile, as shown in Fig. 2 of Pesenti et al. (2004). However, the ionization distribution in the disk wind has a crucial effect on the line profile shape, with, e.g., the peak shifting from high to low velocity depending on whether ionization decreases or increases outward (Pesenti et al. 2004). Therefore, double-peaked profiles could in principle be produced in a single disk wind if ionization conditions are highly inhomogeneous between inner and outer streamlines, e.g. because of localized shocks. To better constrain the respective origins of the two velocity components noted in [Fe II] by Pyo et al. (2003), additional constraints are again needed.

In this paper, we present spectro-imaging of the DG Tau jet in the H-band that provide the first images of this jet in [Fe II] at $\simeq 0.''15$ resolution over a full field of view of $\pm 1.''5$ from the star. This enables us to clarify the morphology and opening angles of the two [Fe II] velocity components identified by Pyo et al. (2003) in long-slit spectroscopy. We also identify new knots and bubble features in both the jet and counterjet, and derive the electronic density distribution along the jet, using the [Fe II] 1.53 μm/1.64 μm ratio. The observations and data reduction are presented in Sect. 2, and our results in terms of morphology,

kinematics, collimation, red/blue asymmetry, disk occultation, and jet densities are presented in Sect. 3. In Sect. 4 we use these results to revise the timescale for knot formation in the DG Tau jet, measure iron depletion in the two velocity components identified by Pyo et al. (2003) and estimate their mass-flux and ejection to accretion ratio. These results are compared to proposed ejection processes in T Tauri stars, in particular the X-wind model (Shang et al. 1998) and the extended MHD disk wind model invoked to fit the rotation signatures in DG Tau (Pesenti et al. 2004). Our conclusions are summarized in Sect. 5.

2. Observations and data reduction

Spectro-imaging observations of the DG Tau microjet in the H- and K-bands were conducted on 2005 October 15 at the Very Large Telescope (VLT) with the integral field spectrograph SINFONI combined with an adaptive optics (AO) module (Eisenhauer et al. 2003; Bonnet et al. 2004). We used a spatial sampling of $0.''05 \times 0.''1$, with the smallest spaxel dimension aligned at PA = 315°, i.e. in the direction transverse to the jet axis, denoted x-axis in the following. This provided a total field of view of about $3'' \times 3''$. The spectral resolution was $\Delta\lambda/\lambda \sim 3000$ in the H-band and $\Delta\lambda/\lambda \sim 4000$ in the K-band, with a spectral sampling of 35 km s^{-1}/pixel and 34 km s^{-1}/pixel in H and K respectively. In the H-band, individual short exposures of 15 s were coadded to build a final datacube with total integration time of 2×270 s on the object and 270 s on the sky. Thanks to AO correction, the effective spatial resolution achieved is $\sim 0.15''$ $FWHM$ in the PSF core (estimated from the reconstructed continuum image).

The data reduction process is common to the two spectral bands. Data reduction steps were carried out with the SINFONI pipeline. Datacubes were corrected for bad pixels, dark, flatfield, geometric distortions on the detector, and sky background. The combined datacube was resampled to a 50 mas × 50 mas square spatial grid. A raw wavelength calibration based on daytime arclamp exposures is performed by the pipeline. However, the accuracy of this calibration (on the order of 50 km s^{-1}) is insufficient for our kinematical jet studies. For the [Fe II] 1.64 μm line, we improved this wavelength calibration locally using the bright OH sky emission line at $\lambda 1.6692$ μm to obtain a 2D wavelength solution over our whole field of view. We estimate a final calibration error in velocity of 10 km s^{-1} rms in this line. The wavelength scale was converted into the stellar rest frame velocity scale. Unfortunately, for the [Fe II]$\lambda 1.53$ μm line, nearby OH lines have a signal-to-noise ratio that is too low to improve wavelength calibration. Therefore, only velocity-integrated 1.53 μm line fluxes are used in the analysis. The data were flux-calibrated on the A2V standard star HIP 26686 in the H-band. We estimate an error in the flux calibration of 5%. Correction for telluric absorption lines was performed together with our continuum subtraction routine (see below). To correct for differential atmospheric diffraction and ensure proper registering, the final datacube for each line of interest is spatially recentered on the centroid position of the local continuum.

The bright stellar spectrum is strong over most of the field of view. In particular, a strong photospheric line is located under the [Fe II] 1.64 μm transition. To better retrieve the intrinsic [Fe II] jet emission profile, especially close to the central source, we performed a specific continuum subtraction, illustrated in the bottom row of Fig. 1. We selected a high signal-to-noise reference photospheric spectrum free of jet emission in the SINFONI field of view (at $\Delta x = 0.054''$, $\Delta y = -0.003''$). This reference spectrum was then scaled down to fit the local continuum level and
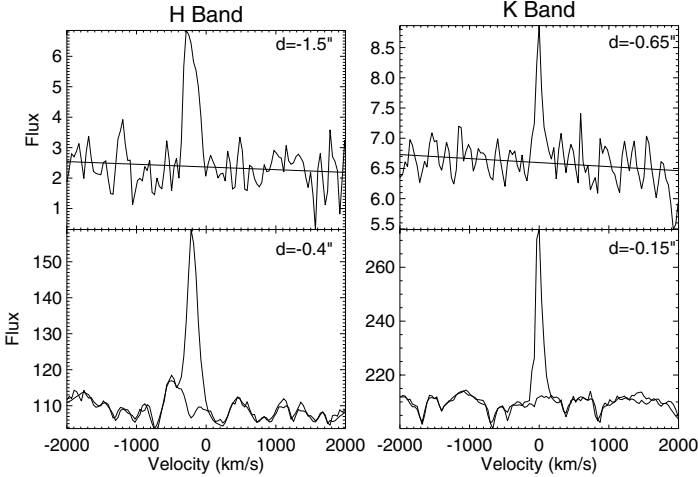
Fig. 1. Illustration of the continuum substraction methods, close to the star (*bottom row*) and far from the star (*top row*), for the [Fe ɪɪ] 1.64 μm (*left panels*) and the H$_2$ 2.12 μm line (*right panels*). The raw spectra are plotted in thick lines and the fitted continua in thin lines. See text for details. The analysis and discussion of H$_2$ 2.12 μm lines will be presented in a separate paper.

was subtracted out from the current spectrum. The high quality of this continuum-fitting procedure can be seen in the bottom row of Fig. 1. It allows us to retrieve the extended jet emission features down to 0″.2 from the star. Furthermore, the residual emission line profile is not only free of photospheric absorption lines but also of telluric features against the continuum, because the depth of telluric absorption scales in proportion to the local flux level[1]. Farther from the star, where the line-to-continuum ratio becomes high, this procedure only provides a partial correction for telluric absorption. However, the telluric absorption depth is less than 7% locally around the [Fe ɪɪ] lines of interest, therefore the error in the emission-line flux is comparable to the flux-calibration uncertainties. At distant positions, where the signal to noise in the stellar continuum is too low for proper continuum scaling, a simple linear baseline is fitted to the local continuum around the line and subtracted (top row in Fig. 1). At each position, we also estimate a spectral noise from the standard deviation of the residual (continuum-subtracted) spectrum on either side of the line. The same continuum subtraction procedures were applied to the H$_2$ 2.12 μm line in the *K*-band. The results in H$_2$ will be presented in a separate paper.

3. Results

The present *H*-band SINFONI data provide the first observations on sub-arcsecond scales of the 2D spatio-kinematic structure of [Fe ɪɪ] emission in the DG Tau jet. Below, we present in turn several new results obtained from our data:

- the [Fe ɪɪ] jet morphology and collimation in various velocity intervals;
- the kinematic structure and variability of [Fe ɪɪ] emission, compared to earlier observations in [Fe ɪɪ] and optical lines;
- the red/blue asymmetry and constraints on the occulting disk;

- the electronic density distribution derived from the [Fe ɪɪ] 1.53 μm/1.64 μm ratio.

3.1. 2D morphology in [Fe ɪɪ]

We show in the top row of Fig. 2 the raw continuum-subtracted [Fe ɪɪ] channel maps reconstructed from our datacube. The emission in each jet lobe was separated in two velocity ranges, chosen to correspond best to the two kinematical components at −200 km s^{-1} and −100 km s^{-1} spectrally identified by Pyo et al. (2003) in their 2001 [Fe ɪɪ] long-slit spectrum along the jet axis[2]. The velocity intervals are the following: high-velocity blueshifted (HVB) = [−300, −160] km s^{-1}, medium-velocity blueshifted (MVB) = [−160, −50] km s^{-1}, medium-velocity redshifted (MVR) = [−50, 120] km s^{-1}, high-velocity redshifted (HVR) = [120, 260] km s^{-1}. Because of our moderate velocity resolution and the lower velocities in the redshifted jet, we extended the MVR channel map to −50 km s^{-1}. The HV channel map shows the sum of the HVB and HVR intervals. The MV channel map shows the sum of MVB and MVR. The blueshifted lobe is at $\Delta y < 0$ in Fig. 2.

The bottom row of Fig. 2 shows the channel maps after deconvolution by a continuum image reconstructed from the same datacube, which provides a good estimate of the point-spread function. We used the LUCY algorithm implemented in the IRAF/STSDAS V3.8 with 40 iterations. We checked that the derived jet morphology (in particular the jet widths) did not change significantly with further iterations. The right-hand panel of Fig. 2 presents a color superposition of the deconvolved HV and MV channels to facilitate comparison between them and to highlight faint emission features.

The deconvolved channel maps reveal several important new features:

(1) the blueshifted [Fe ɪɪ] jet shows a clear increase in collimation at higher flow velocities, with the HVB emission nested inside the MVB emission. This onion-like velocity structure was previously noted in optical lines (Lavalley-Fouquet et al. 2000; Bacciotti et al. 2000), but the unique combination of high resolution and wide transverse coverage provided by SINFONI shows it more clearly. In particular, it confirms the striking conical shape of the MVB emission, which was partly truncated in the narrower HST/STIS channel maps covering ±0″.2 from the jet axis (Bacciotti et al. 2000);

(2) the blueshifted jet contains several knots and bubble-like structures: Two knots are present, one at −0″.37 ± 0.03″ and one at −1″.2 ± 0.05″. The latter is followed by a faint limb-brightened bubble, partly truncated by our field of view, which reaches a maximum width ≃0″.5 around $d \simeq −1″.4$ (see right panel in Fig. 2);

(3) the counterjet emission is dominated by a striking limb-brightened circular bubble centered around ≃+1″. The deconvolved MVR emission is slightly broader and more pointed away from the star than the HVR. No counterjet is detected within 0″.7 from the star. This effect is probably caused by disk occultation (Lavalley et al. 1997; Pyo et al. 2003) and provides interesting constraints on the disk surface density structure in DG Tau (see Sect. 3.4).

---

[1] Our photospheric subtraction procedure would also subtract any *unresolved* [Fe ɪɪ] feature centered *on* the star. However, no such compact component appears to be present in previous high-resolution [Fe ɪɪ] spectra (Pyo et al. 2003).

[2] We will use here the notation MV (medium-velocity) rather than LV for the component at ≃−100 km s^{-1} in Pyo et al. (2003) to be more consistent with the velocity intervals defined in the HST channel maps of Bacciotti et al. (2000); we restrict the use of LV to the component at velocities lower than −50 km s^{-1}, seen in optical lines.
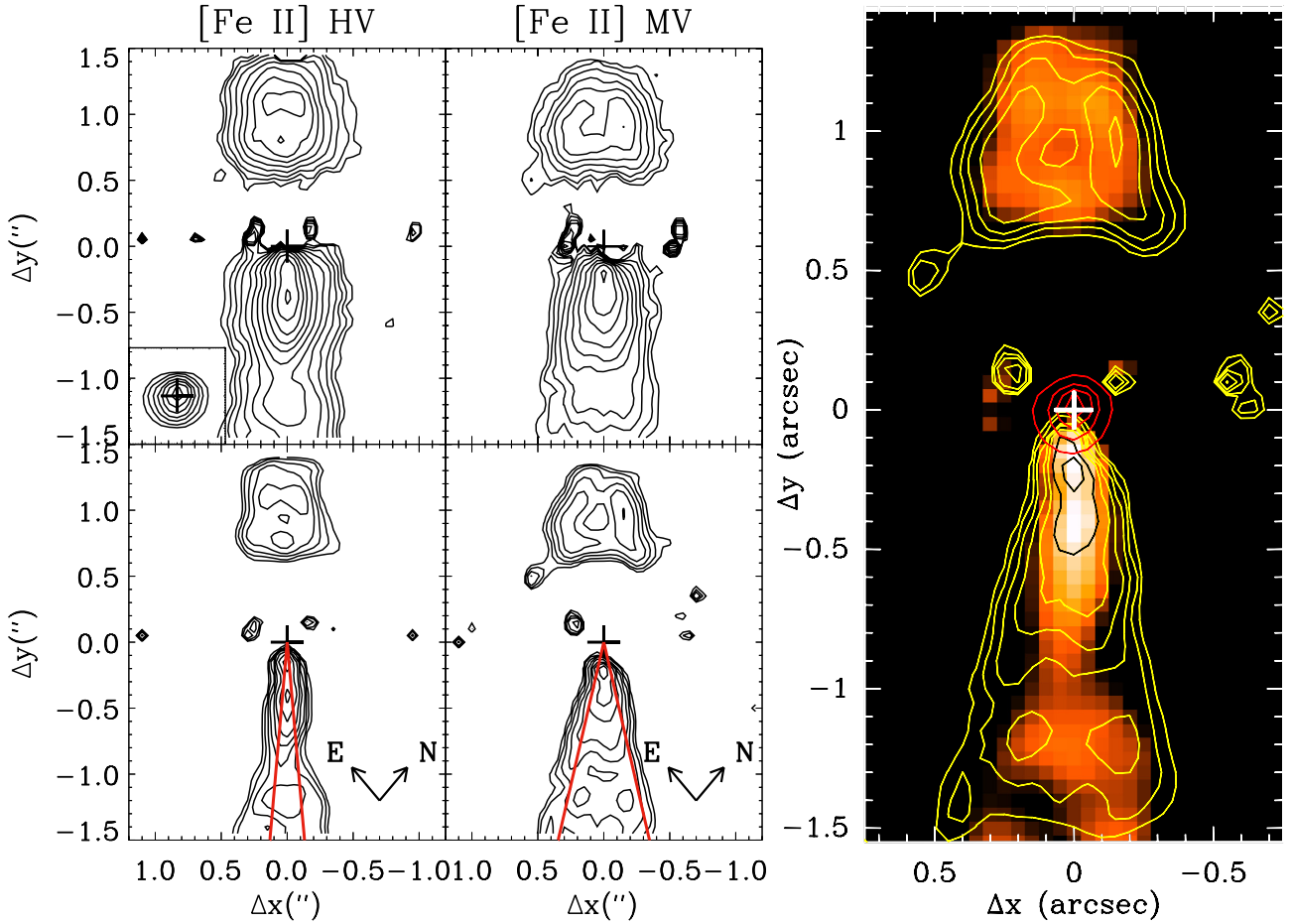
Fig. 2. *Left*: continuum-subtracted [Fe II] 1.64 μm channel maps of the DG Tau jet before (*top panels*) and after (*bottom panels*) deconvolution by the continuum image. The HV channel maps are integrated over the velocity intervals [−300, −160] km s^{-1} (HVB) and [+120,+260] km s^{-1} (HVR); the MV channel map over [−160, −50] km s^{-1} (MVB) and [−50, +120] km s^{-1} (MVR). The blueshifted lobe is at $\Delta y < 0$. The pixel scale is 0.″05. A cross denotes the centroid of the continuum emission (shown as an insert in the top left panel). Contours start at 3σ and increase by factors of $\sqrt{2}$ (lowest contours are 2.0 and 1.8 × 10^{-18} W m^{-2} arcsec^{-2} in the raw HV and MV maps respectively). The solid red lines in the deconvolved maps show the opening angle measured in each component. *Right*: superposition of the deconvolved HV (background color image) and MV (yellow contours) channel maps. The stellar continuum is shown in red contours. The white cross locates the continuum centroid.

3.2. Collimation, opening angle, and upper limits on launch radii

We plot in the left panel of Fig. 3 the jet *FWHM* derived from Gaussian fitting of the transverse intensity profiles in the deconvolved channel maps of Fig. 2. The broader width of the MV channels compared to the HV is clearly visible at all distances. In addition, a widening of the blue jet is seen beyond 1″, corresponding to the faint bubble feature at the end of this lobe. The width there is comparable to the bubble feature in the redshifted lobe.

To estimate intrinsic jet widths and opening angles, we focused on the inner 0.″8 (110 AU) section of the blueshifted lobe, which is least affected by bubble structures. We corrected the measured *FWHM* for the effective PSF width (*FWHM*$_0$) in the deconvolved channel maps with the formula $(2R_{\rm jet})^2 = FWHM^2 - FWHM_0^2$. The effective angular resolution reached in the deconvolved maps cannot be measured precisely because no unresolved point source is present in our (continuum-subtracted) line maps. Therefore we considered a range of possible *FWHM*$_0$ between 0.″05 (pixel scale) and 0.″08 (smallest jet width measured). We plot in the right panel of Fig. 3 the PSF-corrected jet

radii (in AU) in the HVB and MVB channels as a function of distance as well as linear fits to these data points.

We find that the medium-velocity blueshifted (MVB) emission has a conical shape with a roughly constant half opening angle of 14°. The high-velocity blueshifted emission (HVB) keeps a narrow radius (5−10 AU) with a half opening angle of 4° until 0.″8 from the star. The derived opening angles are upper limits because we did not correct for inclination effects. *If these cones traced actual streamlines*, an extrapolation back to the origin would suggest that the HVB component in DG Tau originates in a disk radius <4 AU and the MVB in a disk radius <1 AU. This is compatible with the maximum launch radii of 0.5 AU and 2−3 AU derived from tentative jet rotation signatures at projected flow speeds of −200 km s^{-1} and ≃−50 km s^{-1} respectively (Coffey et al. 2007; Bacciotti 2002; Pesenti et al. 2004). However, it is likely that emission maps in constant velocity bins do not trace actual streamlines especially at low flow velocities. Indeed, outer streamlines are expected to reach their terminal velocities on spatial scales ≃50−100 AU. As a consequence, jet emission radii measured on the MVB channel maps likely underestimate true streamline radii close to the source.
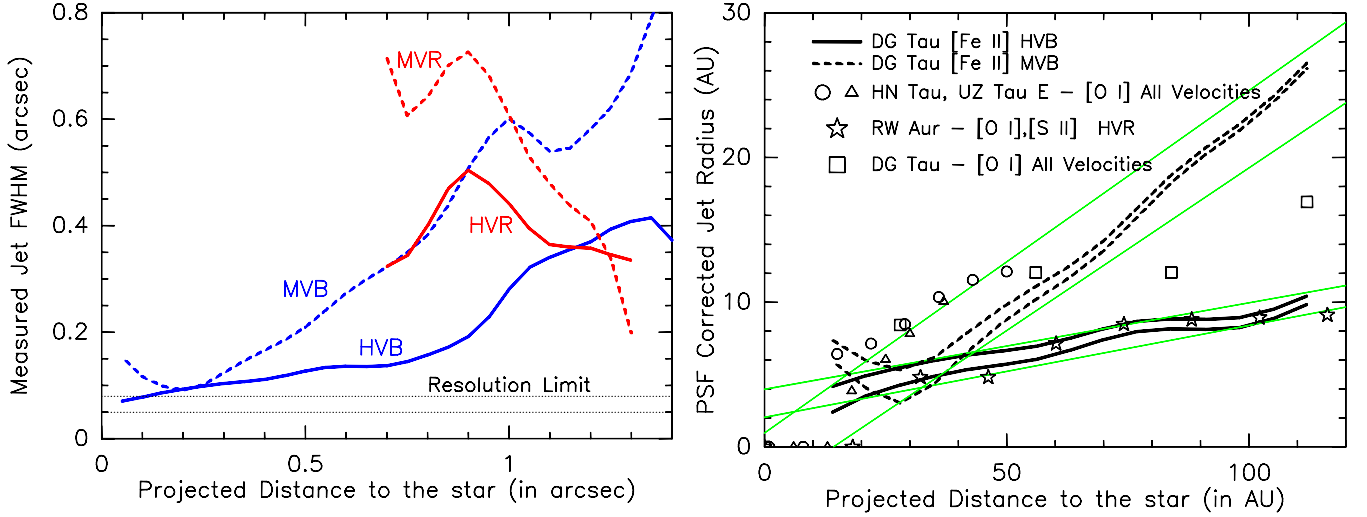
Fig. 3. *Left*: jet *FWHM* derived from Gaussian fits to deconvolved [Fe II] channel maps as a function of projected angular distance from the star. *Right*: PSF corrected (i.e. intrinsic) jet radii as a function of linear distance from the star for the inner $0\farcs8$ of the HVB (solid curves) and MVB (dashed curves). The fitted *FWHM* across the jet were corrected for the angular resolution of $0\farcs05$–$0\farcs08$ in the deconvolved maps by subtracting this PSF in quadrature. Gray/green solid lines show fits by a flow of constant opening angle, suggesting a launch radius smaller than 4 AU (HVB) and 1 AU (MVB). For comparison, open symbols plot jet radii measured in [O I] images integrated over all velocities in DG Tau (open squares Dougados et al. 2000), RW Aur (open stars Woitas et al. 2002), and HN and UZ Tau E (open circles and triangles Hartigan et al. 2004a).

We also compare in Fig. 3 our derived intrinsic jet radii in [Fe II] with previous measurements from *velocity-integrated* [O I] images at similar angular resolution in the RW Aur jet (average of both lobes) (Woitas et al. 2002) and in the HN Tau and UZ Tau E blueshifted jets (Hartigan et al. 2004a). The RW Aur microjet, where [O I] is dominated by a single high-velocity component (Woitas et al. 2002), shows an opening angle and width strikingly similar to the HVB interval in DG Tau. The HN Tau and UZ Tau E [O I] jets, dominated by a medium to low-velocity component (Hartigan et al. 1995), have a much wider opening angle similar to the MVB. Therefore, the increase in collimation at higher velocity seen in DG Tau could be a widespread generic property in T Tauri jets. Finally, we note that the jet widths from a velocity-integrated [O I] image of the DG Tau jet taken in 1997 (Dougados et al. 2000) fall close to the MVB component out to 50 AU, but closer to the HVB beyond 50 AU. Therefore, jet opening angles measured from velocity-integrated images may be misleading when different velocity components dominate at different positions along the jet.

### 3.3. 2D kinematics of the blueshifted jet

To attain an overall view of the 2D jet kinematics, we performed at each spatial position a one-component Gaussian fit to the line profile. Although two kinematical components are clearly present in the jet (as shown by the distinct morphologies of channel maps in the HV and MV velocity ranges), a two-component Gaussian fit did not give coherent results over the field of view because of the moderate spectral resolution of our observations. We show in Fig. 4 the derived 2D map of the fitted centroid velocities. From the formula outlined in Agra-Amboage et al. (2009) and the observed signal-to-noise ratios, we estimate an uncertainty in centroid velocities in the range 14–21 km s^{-1}.

The centroid map shows a clear transverse velocity gradient in both lobes, with the highest flow velocities concentrated toward the axis. The gradient is especially apparent in the blue lobe at distances greater than 0.4″ from the star. This transverse

gradient is consistent with the higher degree of collimation in the HV channel maps and the wider, limb-brightened morphology in the MV channel maps. The centroid values toward the flow edges indicate a mean absolute velocity of ≤ 50 km s^{-1} for the MVR component, and ≤ 100–150 km s^{-1} for the MVB component toward the blue lobe, similar to the low velocity spectral component identified by Pyo et al. (2003) in their 2001 long-slit [Fe II] spectrum, of higher spectral resolution than our data.

Variations of centroid velocities along the jet axis are also seen. They are illustrated in Fig. 4, right panel, where we plot a position-velocity diagram along the jet, reconstructed by averaging our spectra over a 1″ wide pseudo-slit. Transverse-average centroid velocities decrease from -192 km s^{-1} at $-0.4″$ (position of the first knot) down to -150 km s^{-1} at $-0.8″$ and increase again to reach -210 km s^{-1} at the outer knot at $-1.2″$. We note a striking similarity with the amplitude and period of the velocity variations in the high-velocity range reported by Pyo et al. (2003) along the jet, despite the time difference of four years between our observations. When corrected for a jet inclination of 42°, the variation amplitude $\Delta V_{\rm rad} \simeq 40$–$60$ km s^{-1} suggests internal shock speeds $v_{\rm s} \simeq 60$–80 km s^{-1}, similar to the $v_{\rm s} \simeq 50$–70 km s^{-1} inferred in 1998 from optical line ratios in the velocity range $[-250, -100]$ km s^{-1} (Lavalley-Fouquet et al. 2000). In both lobes, the maximum radial velocity is found toward the bubble feature near the edge of our field of view.

One notable difference between our [Fe II] PV diagram and that of Pyo et al. (2003) is that the line flux is dominated by the HVB all the way down to $-0\farcs2$ from the star in our observations (Fig. 4, right panel), whereas it was dominated by the MVB within $0\farcs5$ of the star in 2001 (Pyo et al. 2003). This difference could be caused by the bright high-velocity knot present at $-0\farcs4$ in our SINFONI map, which had not yet – or barely – emerged in 2001 October (see Sect. 4.1). Another difference is the nondetection of the MVB component beyond $0\farcs5$ from the star by Pyo et al. (2003), which may be caused by the narrow slit ($0\farcs3$ width) used in their observations. As shown in Fig. 3, the measured MVB FHWM exceeds $0\farcs3$ beyond $0\farcs6$, therefore
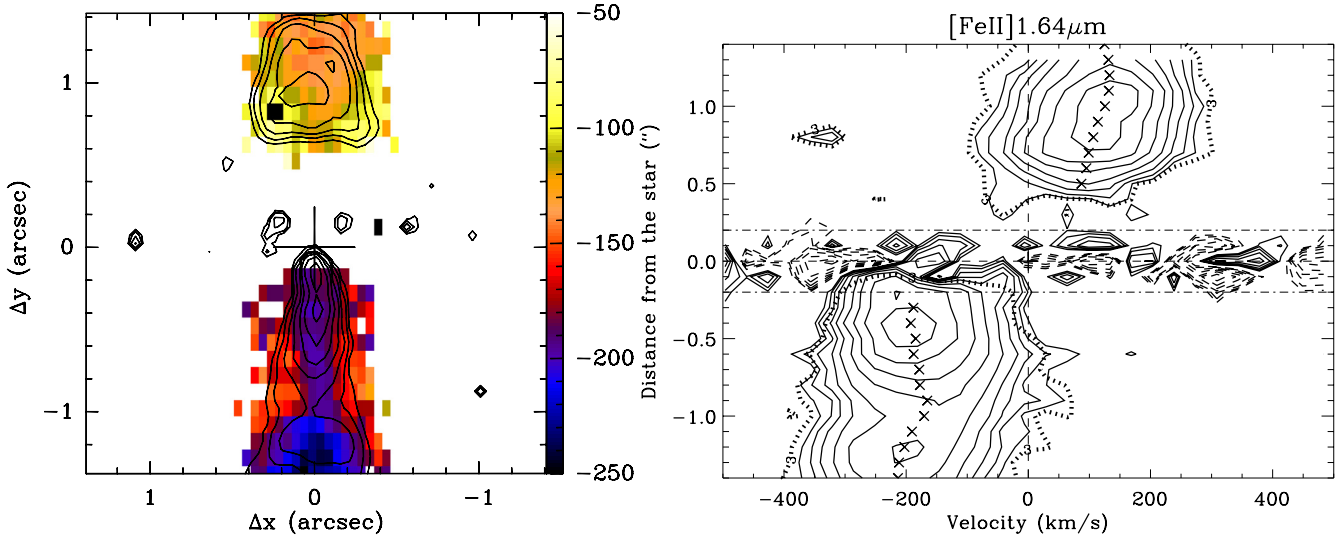
Fig. 4. *Left*: 2D maps of the [Fe II] 1.64 μm velocity centroid deduced from one component Gaussian fitting of the line profile. Redshifted velocities are shown on a negative scale to better highlight the velocity asymmetry between them. Spectra with SNR lower than 5 were masked. The cross marks the location of the continuum. Contours show the sum of the deconvolved HV and MV channel maps. *Right*: PV diagram of [Fe II] along the jet, averaged over $\pm0.''5$ across the jet, with velocity centroids indicated as crosses. Horizontal dash-dotted lines indicate the region where residual noise after continuum subtraction is still large. Contours start at 2.43×10^{-15} W m^{-2} μm^{-1} arcsec^{-2} and increase by factors of $\sqrt{2}$. The 3σ contour is shown as a dotted line.

a significant fraction of the MVB flux has likely been missed at these distances in the Pyo et al. (2003) long-slit observations.

Finally, we note that neither our PV diagram nor that of Pyo et al. from 2001 show [Fe II] emission at velocities faster than -300 km s^{-1} or lower than -60 km s^{-1}, corresponding respectively to the "very high velocity" (VHV) and "low velocity" (LV) components detected in the DG Tau blueshifted jet in optical lines respectively (Lavalley et al. 1997; Lavalley-Fouquet et al. 2000; Bacciotti et al. 2000). HST maps obtained in 1999 show that the VHV optical gas was tracing a bright knot followed by an elongated bubble (Bacciotti et al. 2000). It was therefore produced by an intrinsically transient event, and it is conceivable that new knots probed by the 2001−2005 [Fe II] observations may not have reached these high velocities.

On the other hand, the halo of broad LV emission seen in [O I] and [S II] surrounding the blueshifted DG Tau jet is present in all optical observations since at least 1993 (Lavalley et al. 1997; Lavalley-Fouquet et al. 2000; Bacciotti et al. 2000) and most recently in 2003 (Coffey et al. 2007). Therefore it appears to be an intrinsically stable feature, and its absence in [Fe II] is significant. To illustrate this, we compare in Fig. 5 the transverse PV diagrams of [S II] 6731 Å and [O I] 6300 Å obtained on 2003 December 1 with HST/STIS at $-0.''3$ from the source (Coffey et al. 2007) with a transverse PV diagram in [Fe II] covering the same area, reconstructed from our SINFONI datacube. In optical data, a spatially broad LV component is clearly visible of the centroid decreasing from -60 km s^{-1} on-axis to -30, -40 km s^{-1} at $\pm0.''2$ from the jet axis (Coffey et al. 2007). Similar low speeds were observed at least out to $0.''6$ from the star (see parallel slits S1 and S7 in Fig. 3 of Bacciotti 2002). The weakness/absence of [Fe II] emission from this off-axis LV component is striking. In Sect. 4 we interpret this difference as substantial iron depletion onto dust grains in the low-velocity sheath surrounding the jet.
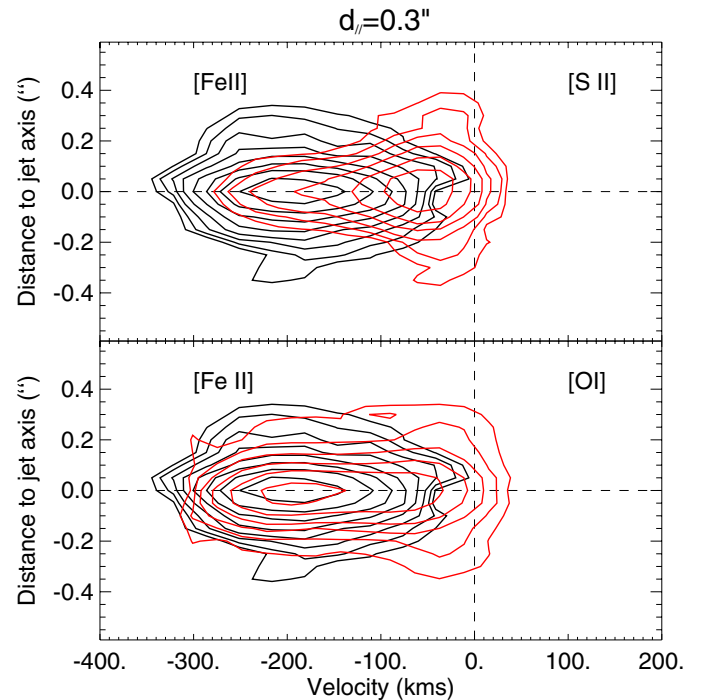
Fig. 5. Comparison of transverse PV diagrams of [S II] 6731 Å and [O I] 6300 Å (red curves) obtained in 2003 with HST/STIS at $d = -0.''3$ from the source in a $0.''1$ wide slit (Coffey et al. 2007, 2008) with a transverse PV diagram in [Fe II] (black curves) at the exact same position, reconstructed from our SINFONI datacube obtained in October 2005. Note the striking lack of [Fe II] emission in the spatially wide low-velocity [O I] component at $V = -30$, -40 km s^{-1}.

3.4. The counterflow: velocity asymmetry and constraint on disk structure

The counterjet emission in our data is dominated by a striking bubble-like structure of similar width and brightness as the
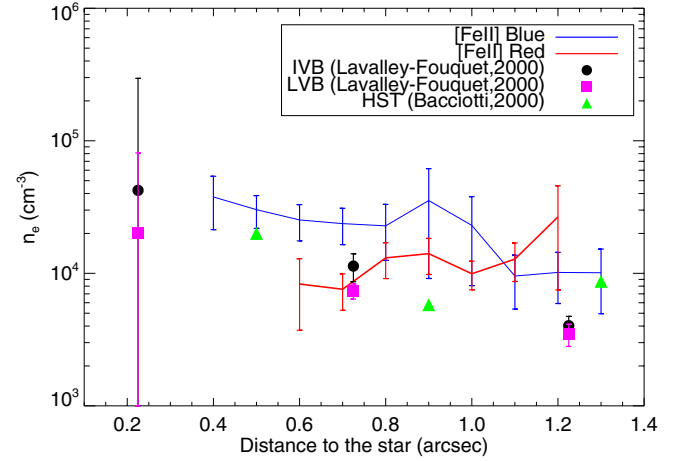
bubble partially imaged in the blueshifted jet (see Figs. 2, 3). On the other hand, the velocity centroid map presented in Fig. 4 reveals a clear velocity asymmetry between the red and blue bubbles. The maximum measured radial velocity centroid toward the red bubble is $\simeq +160$ km s^{-1}, i.e. only 70% of the peak velocity $\simeq -230$ km s^{-1} in the blue bubble. This velocity asymmetry is consistent with the 70% smaller distance from the star to the center of the redshifted bubble, compared to the (approximate) center of its blueshifted counterpart ($\simeq +1''$ versus $-1''.4$). This agreement suggests that both bubbles were generated in a simultaneous ejection event.

The red/blue asymmetry in velocity and position needs to be taken into account when quantifying the dust extinction produced by the DG Tau disk toward the counterjet. In October 2001, Pyo et al. (2003) detected only very weak[3] redshifted [Fe II] emission around $0''.9$, 10 times weaker than their blueshifted jet at the same distance from the star. They inferred an extinction of 2.5 mag at H at this distance, assuming intrinsically equal brightnesses. If one corrects for the differential speeds and compares instead with their blueshifted jet intensity at $0''.9/0.7 = 1''.3$, the relative intensities become comparable, suggesting negligible extinction by the disk at $1''$. This result is much more consistent with the similar brightness of the red and blue bubbles in our SINFONI data.

The deconvolved [Fe II] channel maps suggest that the central obscuration of the redshifted jet from the disk extends to projected angular distances of $d \simeq 0''.7$, i.e. 140 AU in deprojected disk radius (assuming a distance of 140 pc and a disk inclination of 42°). This requirement appears to set constraints on models of the disk density distribution in DG Tau derived by Isella et al. (2010) from sub-arcsecond millimeter continuum interferometric maps. In particular, it seems inconsistent with a single power-law surface density distribution, which requires a small outer disk radius of 70–80 AU to fit DG Tau observations (Isella et al. 2010). Such a small disk radius would produce no extinction beyond $0''.4$ from the star, unlike SINFONI observations. An alternative similarity solution with an exponential tail fitted to the mm map predicts a (perpendicular) surface density of $\Sigma = 0.25{-}1.5$ g cm^{-2} at a disk radius of $r = 100$ AU (Isella et al. 2010), leading to $A_H = 30{-}5$ mag at $d = 0''.5$ assuming interstellar dust extinction, with Σ and therefore A_H dropping by a factor $\simeq 10$ at $d = 0''.7$ ($r = 140$ AU). The similarity solution for the surface density distribution therefore appears more consistent with the central obscuration observed in the SINFONI maps.

3.5. Electron density in the [Fe II] emitting region

The ratio R of the [Fe II] 1.53 μm to 1.64 μm lines is a good diagnostic of the electronic density n_e in the range $10^3{-}10^5$ cm^{-3} (Pradhan & Zhang 1993). The temperature dependence of R is weak in the range $T_e \simeq 8000{-}20\,000$ K encountered in the forbidden-line emission regions of stellar jets (e.g. Bacciotti & Eislöffel 1999). We did not detect any change in this ratio across the line profile nor across the jet width at our resolution. Therefore we computed at each spatial distance along the jet a mean [Fe II] line ratio integrated over all velocities and over $\pm 0''.5$ from the jet axis. The flux for each line was obtained by fitting it to a Gaussian and then integrating over all velocities. Errors in

---

[3] The redshifted bubble was probably at that time entirely hidden behind the high-extinction region close to the star. Assuming a proper motion of 70% that of the blueshifted knots ($\simeq 0''.3$/yr, see Sect. 4.1) the tip of the redshifted bubble projected at $1''.3$ arcsec from the star in October 2005 would have been at $0''.46$ in October 2001.

Fig. 6. Plot of n_e versus distance derived from the ratio of the [Fe II] 1.53 μm to 1.64 μm lines (averaged over $\pm 0''.5$ from the jet axis) for the blueshifted (blue points, top curve) and redshifted (red points, bottom curve) lobe. Also shown are previous determinations from the [S II] doublet ratio over similar velocity ranges: IVB and LVB from Lavalley-Fouquet et al. (2000) (black circle, purple square), MVB interval of Bacciotti et al. (2000) (green triangles).

the Gaussian parameters are derived taking into account observational errors on the spectral profile and propagated to obtain the final errors on the derived ratio. We then derived the electronic density from the observed line ratio using the theoretical relation between R and n_e at a temperature $T_e \simeq 10\,000$ K, calculated from the 16-level Fe$^+$ model of Pesenti et al. (2003). For ratios R between 1.0 and 3.9, this relation can be fitted analytically within an accuracy of 20% on n_e by

$$n_e(R) = 1.2 \times 10^4 \times (R - 0.035)/(0.395 - R) \quad \text{cm}^{-3}. \qquad (1)$$

The n_e values as a function of distance along the jet are presented in Fig. 6. For comparison, we also plot in Fig. 6 earlier n_e determinations obtained in January 1998 and 1999 from the optical [S II] 6716, 6731 ÅÅ doublet ratio over a similar velocity range: namely, the IVB $[-250, -100]$ km s^{-1} and LVB $[-100, +10]$ km s^{-1} intervals of Lavalley-Fouquet et al. (2000), and the MVB $[-195, -72]$ km s^{-1} interval of Bacciotti et al. (2000). The HVB $[-319, -195]$ km s^{-1} interval of Bacciotti et al. had a saturated ratio indicating electronic densities $\gg 10^4$ cm^{-3} out to $1''.4$.

This comparison shows that the overall n_e distribution along the blueshifted DG Tau jet has remained remarkably similar in the velocity range $[-300, +10]$ km s^{-1} between 1998 and 2005, with a general increase of only a factor 2 over this period. The actual change in total flow density, n_H, would be even smaller than a factor 2 if the ionization fraction had increased over this time period or if the [S II] 6716, 6731 ÅÅ doublet were biased toward less dense jet regions than [Fe II], as found by Nisini et al. (2005). We will take advantage of this small variability level to estimate iron gas-phase depletion in Sect. 4.2.
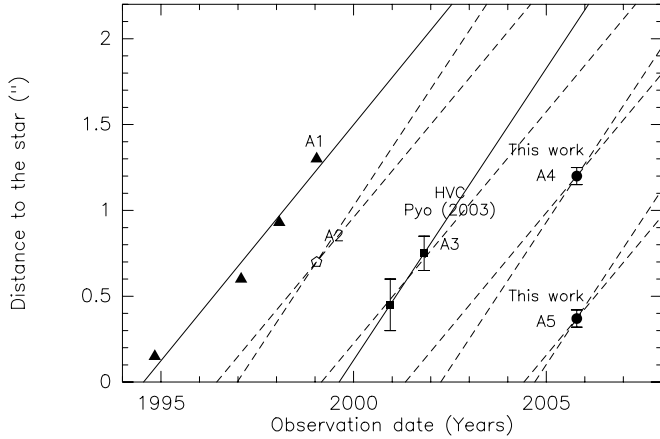
4. Discussion

Below, we analyze our SINFONI results and discuss the resulting implications concerning

– the timescale for knot and bubble formation;
– the gas-phase iron depletion in the blueshifted jet;

Fig. 7. High-velocity knot position versus observing date in the DG Tau blueshifted jet updated from Fig. 5 of Pyo et al. (2003). Solid lines show the proper motions derived by Pyo et al. (2003) for knots A1 and A3. For knots with only one epoch, dashed lines show the typical proper motion range of 0.″27 yr⁻¹–0.″34 yr⁻¹. The two new knots observed with SINFONI and knot A2 observed with HST indicate that a new knot typically emerges every 2.5 years since 1991. References for knot positions may be found in Table 1 of Pyo et al. (2003).

– the jet mass-flux and ejection to accretion ratio;
– the proposed ejection processes and launch radii in DG Tau.

4.1. Period of knot generation in the DG Tau jet

Pyo et al. (2003) investigated the knot proper motions and ejection timescales in the DG Tau blueshifted lobe from 1991 to 2001, using a compilation of data from the literature. They concluded that a new knot emerges every five years. Here we re-examine this matter and show that the SINFONI data indicate half that timescale.

The HVB emission map reveals two well defined [Fe II] emission knots at distances from the star of $-0.''37 \pm 0.03''$ and $-1.''2 \pm 0.''05$. In Fig. 7 we add these two HVB knots onto the distance-date diagram of Pyo et al. (2003, their Fig. 5). We also plot the proper motions determined by Pyo et al. (2003) for knot A1 (0.″275 yr⁻¹ from four epochs) and for their HV peak (0.″34 yr⁻¹ from two epochs). We denote the latter A3, extending the knot-naming convention introduced by Bacciotti et al. (2000).

Evidently, the two high-velocity knots identified in our HVB map correspond to new ejection events: the HV knot A3 should lie at $\simeq -2''$ at the time of our observations, i.e. well outside of the SINFONI field of view. If we assume for these new knots A4 and A5, and for the previous knot A2, proper motions in the same range 0.″27–0.″34 yr⁻¹ as found for A1 and A3, we derive intervals between knots of about 2.5 yrs between 1995 and 2005 (typical spacing between knots of 0.75″ in the blue lobe). Our observations therefore suggest the presence of a knot variability timescale a factor two shorter than derived by Pyo et al. (2003). We note that the bubble structures observed in our SINFONI images appear to have formed in the wake of the same ejection event as HV knot A3: if we adopt a proper motion in the red lobe of 70% of the mean proper motion of 0.″3 yr⁻¹ in the blue lobe, as suggested by the red/blue asymmetry (see Sect. 3.4), the position of the tip of the red bubble at +1.″3 from the star in October 2005 yields an ejection date around August 1999, the same as for knot A3. The formation of a bubble structure in the wake of a knot has been previously seen in the case

of knot A1 in HST images (Bacciotti et al. 2000). It may thus be a common feature in DG Tau.

We did not include the MV knot identified by Pyo et al. (2003) in our timescale analysis because the estimated proper motion of 0.″28 yr⁻¹ yields a ratio of proper motion to radial velocity 60% higher compared to the HV knot. This is not consistent with ballistic motions of a gas parcel along the jet axis, which would predict a constant ratio of proper motion to radial velocity (equal to tan(*i*), with *i* the jet inclination to the line of sight). Therefore the MV knot of Pyo et al. does not appear to trace a separate ejection event, but rather a brightness enhancement following the HV knot A3.

4.2. Iron depletion in the blueshifted jet

The dust content of stellar jets is a key parameter in determining whether the outflowing material originates inside or outside the dust sublimation radius. The gas phase depletion of refractory species such as Fe or Ca, measured with respect to the solar abundance, offers a direct indication of the presence of dust in the jet. In previous studies of HH jets by Nisini et al. (2002, 2005); Pesenti et al. (2004); Podio et al. (2006, 2009), relatively high Fe and Ca gas-phase abundances of 20%–80% the solar value were inferred, but most of these observations probe relatively large distances from the driving sources ≥10″, where the original dust content of the flow may have been modified, e.g. through dust destruction in shocks. Exceptions are Nisini et al. (2005) and Podio et al. (2009) who reported Fe and Ca depletions at 1–3″ of the source in the HH 1 and HH 24 jets, corresponding to 450–1300 AU at the distance of Orion. Our sub-arcsecond resolution SINFONI observations of the DG Tau jet in [Fe II] provide the first opportunity to constrain the dust content of the blueshifted jet down to only 50 AU (0.″3) from its driving source, i.e. much closer than achieved in previous depletion studies of HH jets.

Iron depletion is estimated by comparing [Fe II] fluxes with lines from species that show little or no depletion onto grains, such as sulfur (Beck-Winchatz et al. 1996; Pesenti et al. 2003), oxygen (Mouri & Taniguchi 2000), hydrogen (Nisini et al. 2002), or phosphorus (Podio et al. 2006). Because our SINFONI data include no lines from the above species, we use here previous flux-calibrated [O I]λ6300 Å observations of the inner regions of the DG Tauri blueshifted jet obtained in January 1998 by Lavalley-Fouquet et al. (2000) with OASIS/CFHT with an angular resolution of 0.″4 and a velocity resolution of 90 km s⁻¹.

We show in Fig. 8 the [Fe II] 1.64 μm/[O I] 6300 Å line ratios derived from integration of our data over the same velocity intervals IVB[–250, –100] km s⁻¹ and LVB[–100, +10] km s⁻¹ and the same distance ranges along the jet as used by Lavalley-Fouquet et al. (2000): $d_{\parallel} = -0.''225, -0.''725, -1.''225$, with pixel size of 0.″5 along the jet. These ratios are plotted against the 1.53 μm/1.64 μm ratio, averaged over the same velocity and distance intervals.

In the bottom and top panels of Fig. 8 we compare there with predictions for a solar abundance ratio Fe/O = 0.062 (Asplund et al. 2005) in two excitation cases: (i) a stratified planar shock wave (denoted "shock method" hereafter), and (ii) an emitting volume of homogeneous density and temperature (denoted "volume method" hereafter).

For atomic shock waves, we considered the models presented in Hartigan et al. (2004b), covering preshock densities $n_H = 10^3 - 10^5$ cm⁻³, shock speeds of 30–50 km s⁻¹, a preshock ionization fraction of 1%–50%, and a preshock magnetic field of
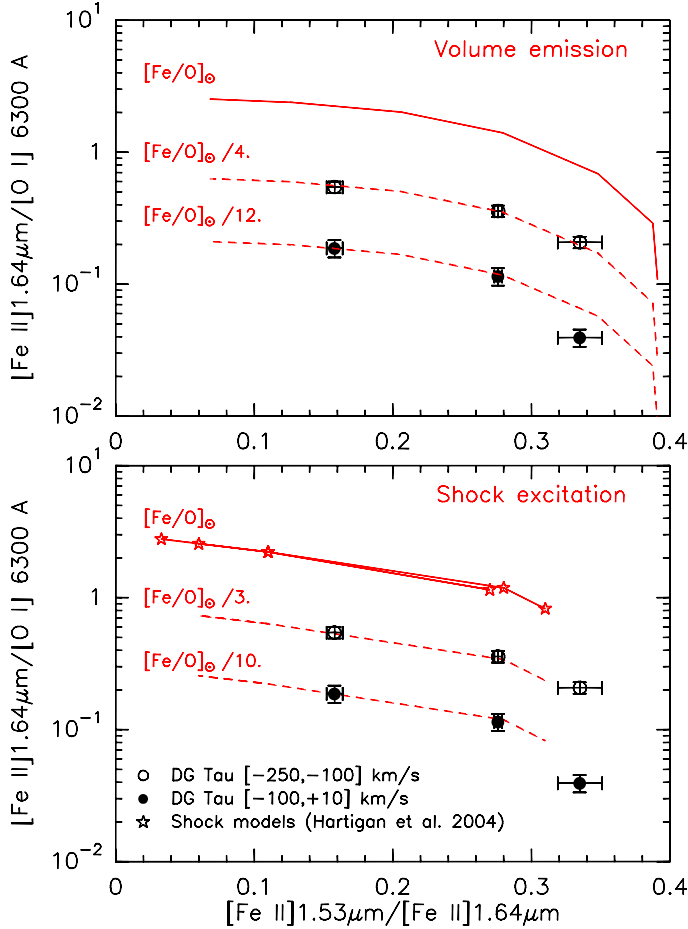
Fig. 8. Line ratio diagnostic diagram for Fe gas phase depletion: [Fe II] 1.64 μm/[O I] 6300 Å versus [Fe II] 1.53/1.64 μm. [Fe II] line fluxes are integrated over the same velocity and spatial intervals as [O I] fluxes from Lavalley-Fouquet et al. (2000). The three data points correspond to distances along the DG Tauri blueshifted jet of 0''.25, 0''.75 and 1''.25 (increasing with decreasing [Fe II] 1.53/1.64 μm). Full curves show predictions for volume emission at 8000 K (*top panel*) and for J-shocks (*bottom panel*) from Hartigan et al. (2004b) assuming an [Fe/O] solar gas phase abundance of 0.062 (Asplund et al. 2005). Dashed curves show [Fe/O] abundances required to reproduce observed line ratios. They indicate Fe gas phase depletion by a factor 3–4 for the IVB[–250, –100] km s^{-1} and 10–12 for the LVB[–100, +10] km s^{-1} intervals.

30–200 μG. We find that the observed [Fe II]/[O I] line ratios in the DG Tau jet are systematically lower than the predictions for a solar Fe/O ratio, by a factor 3 in the IVB interval and by a factor 10 in the LVB interval, independent of the distance from the source. Note that the predicted line ratio curve assumes that the mass-flux entering the shock was the same in 1998 ([O I] data) and 2005 ([Fe II] data), i.e. that the twice higher electronic density in [Fe II] in 2005 compared to [S II] in 1998 (Sect. 3.5) is mostly caused by ionization gradients within the shock cooling zone. This gives a conservative lower limit to iron depletion. If, instead, the increase in n_e between the [O I] and [Fe II] observations were caused by an increase in pre-shock density, one would predict a higher [Fe II]/[O I] ratio and infer a larger iron depletion in the jet.

For the uniform volume method, assumptions need to be made on the temperature and ionization state of the gas: we assume a temperature of 8000 K typical of stellar jets, that iron is all in the form of Fe$^+$ and oxygen is mostly neutral (as expected at such temperatures). The predicted [Fe II]/[O I] ratio assumes

that the mass in each element of volume was about the same between 1998 and 2005, i.e. that the difference in n_e between the two data sets is caused by an increase in ionization fraction between the two epochs. The results are remarkably similar to the shock method: an Fe/O ratio lower than solar by a factor 4 in the IVB interval and a factor 12 in the LVB interval. Again, inferred depletions would increase if the total jet density n_H (instead of x_e) increased between the two epochs. Finally, we note that applying an extinction correction to the observed line fluxes would decrease the observed [Fe II]/[O I] ratio, again increasing the inferred depletion in both methods.

To evaluate a possible effect of time variability in the [O I] line, we compared the [O I] fluxes measured in 1998 by Lavalley-Fouquet et al. (2000) against the flux-calibrated HST/STIS transverse PV diagram obtained on 2003 December 1 at a distance of –0''.3 from the star (Coffey et al. 2007). The [O I] line fluxes per arcsecond length of the jet in the IVB and LVB intervals in the latter data (1.9×10^{-13} and 1.3×10^{-13} erg s^{-1} cm^{-2} arcsec^{-1} respectively; Coffey, priv. comm.) are 80% and 5% higher than their respective values in December 1998 at the same distance, averaged over 0''.5 along the jet. Using the Coffey et al. [O I] fluxes would thus increase depletion in the IVB range at 0''.3 by a factor 2, while depletion in the LVB would remain unchanged. However, line fluxes measured in the narrow HST slit (of width 0''.1) will also be more affected by the precise position of knots at the epoch of observation than fluxes averaged over 0''.5 along the jet. Results obtained by comparison with Lavalley [O I] data may thus be more reliable despite the longer time span.

We thus tentatively interpret the low [Fe II]/[O I] ratios observed as indication of iron gas-phase depletion by a factor ≃3–4 in gas faster than –100 km s^{-1} and by a factor of 10–12 at speeds below –100 km s^{-1}. This would correspond to about 33% and 10% of elemental iron in the gas phase, respectively. Simultaneous observations of the DG Tau jet involving refractory and non-refractory species would be extremely valuable to confirm the present findings. The observed trend of higher depletion at lower flow velocities, also seen in Podio et al. (2009) in calcium toward the HH 111 jet, would imply that slower jet material in the jet originates in regions farther from the star than higher velocity material, or that it has been less shock-processed. Implications for launching models are discussed in Sect. 4.5.

4.3. Blueshifted jet mass-flux in the [Fe II] emitting components

From our [Fe II] observations we derive estimates of the mass-flux rates in the atomic component of the blueshifted jet as a function of the distance from the star, and for the two velocity intervals HVB and MVB. We used three different methods, the first one based on estimates of the jet density and cross-section, the other two based on the [Fe II] luminosity, corrected for depletion. We detail below the assumptions and parameters for these three methods. The resulting mass-fluxes are plotted as a function of distance in Fig. 9.

4.3.1. Method 1: from jet density and cross-section

For a jet of cross-section A_J and velocity V_J, uniformly filled with a density of hydrogen nuclei n_H, the mass-flux rate is given by

$$\dot{M}_J = \mu m_H n_H A_J V_J,$$

where μ, the average weight per hydrogen nucleus, is 1.4 for a cosmic gas with 10% helium. Assuming a circular cross section

of diameter D_J, the above equation can be re-written as

$$\dot{M}_J = 1.3 \times 10^{-9} \, M_\odot \, \text{yr}^{-1} \left(\frac{n_H}{10^5 \, \text{cm}^{-3}}\right) \left(\frac{D_J}{14 \, \text{AU}}\right)^2 \left(\frac{V_J}{100 \, \text{km s}^{-1}}\right). \tag{2}$$

This method has the advantage of being unaffected by iron depletion or by circumstellar extinction. We plot in Fig. 9 (dashed-dotted line) the mass-loss rates derived from this method and computed every $0\rlap{.}''1$ along the blueshifted jet.

We used an average deprojected velocity $V_J = 300 \, \text{km s}^{-1}$ for the HVB and $V_J = 135 \, \text{km s}^{-1}$ for the MVB ranges, derived from the average radial velocities of $V_r \simeq 220$ and $100 \, \text{km s}^{-1}$ of the spectral components resolved by Pyo et al. (2003), with a jet inclination angle with respect to the line of sight of $i = 42°$ Lavalley (2000). To estimate the HVB cross-section, we took $D_{\text{HVB}}^2 = FWHM_{\text{HVB}}^2 - FWHM_0^2$ where $FWHM_{\text{HVB}}$ is the transverse [Fe II] emission width measured in the HVB deconvolved maps, and $FWHM_0 = 0\rlap{.}''05-0\rlap{.}''08$ is the effective resolution of these maps. To estimate the cross-section of the MVB flow, we subtracted the cross-section of the central HVB component nested inside it, i.e. we take $D_{\text{MVB}}^2 = FWHM_{\text{MVB}}^2 - FWHM_{\text{HVB}}^2$. The effective resolution of the deconvolved maps cancels out in this case.

Estimates of the total density n_H along the jet are derived from n_e/x_e, where the electronic densities n_e along the jet are obtained from our [Fe II]1.533/1.644 line ratios. For the hydrogen ionization fraction x_e, we used linear fits to the values derived by Bacciotti (2002) in 1999 with HST/STIS from optical line ratios on similar spatial scales and velocity ranges. One potential limitation in using these values may come from time variability. However, the x_e values obtained in 2003 at $d = -0\rlap{.}''3$ by Coffey et al. (2008) agree very well with the 1999 values of Bacciotti (2002), indicating moderate variability on a three year timescale in this parameter. Our mass-flux estimates at $d = -0\rlap{.}''3$ in the HVB and MVB intervals differ slightly from those obtained by Coffey et al. (2008) using the same method (star symbols in Fig. 9), the discrepancy mainly comes on the one hand from a jet radius twice as large as our estimate (they do not correct for instrumental PSF) and because of the quadratic dependence, this results in a factor 4. On the other hand, the total density obtained by Coffey et al. (2008) is a factor 3 lower than ours, which compensates the factor 4 from the jet width. The difference in MVB also arises because the authors do not correct the MVB width by the area filled by the HVB, which we do.

4.3.2. Method 2: from [Fe II] luminosity, volume emission from uniform jet slab

The second method derives the mass-loss rate from [Fe II] 1.64 μm luminosities assuming optically thin volume emission from a uniform jet slab. This method, described in detail in Hartigan et al. (1995) for optical lines, assumes uniform T_e, x_e and n_e and relates the line flux to the emitting mass within the elementary aperture. Using a 16-level excitation model of Fe$^+$ (Pesenti et al. 2003), we fitted the emissivity of the 1.64 μm line as a function of n_e for $T_e \simeq 10^4$ K as

$$j(1.64 \, \mu\text{m}) = 2 \times 10^{-17} \times \left(1 + \frac{3.5 \times 10^4}{n_e(\text{cm}^{-3})}\right)^{-1} \, \text{erg s}^{-1} \, \text{sr}^{-1} \, \text{ion}^{-1} \tag{3}$$

(a good approximation for $n_e \geq 3000 \, \text{cm}^{-3}$). The mass-loss rate is then given by the mass divided by the pixel crossing time

$$\dot{M}_J = 1.45 \times 10^{-8} \, M_\odot \, \text{yr}^{-1} \left(1 + \frac{3.5 \times 10^4}{n_e(\text{cm}^{-3})}\right) \left(\frac{L_{[\text{FeII}]}}{10^{-4} \, L_\odot}\right)$$
$$\times \left(\frac{V_t}{150 \, \text{km s}^{-1}}\right) \left(\frac{l_t}{2 \times 10^{15} \, \text{cm}}\right)^{-1} \left(\frac{[\text{Fe/H}]}{[\text{Fe/H}]_\odot}\right)^{-1}, \tag{4}$$

with l_t the size in the plane of sky of the elementary aperture along the jet axis, V_t the tangential flow velocity in the plane of sky, and $[\text{Fe/H}]_\odot = 2.82 \times 10^{-5}$ (Asplund et al. 2005).

We computed the [Fe II] 1.64 μm luminosity in the HVB and MVB channel maps in rectangular apertures of projected length along the jet axis $l_t = 0.1'' = 2 \times 10^{14}$ cm (at 140 pc), and width $\pm 0\rlap{.}''5$ across the jet. We adopted the same values of n_e as a function of distance as in method 1 and the same radial velocities to derive $V_t = V_r \times \tan(i)$. Finally, we applied the correction for the Fe gas-phase depletion estimated in the previous section, using the "volume" hypothesis, $[\text{Fe/H}]/[\text{Fe/H}]_\odot = 1/4$ and $1/12$ for the HVB and MVB respectively. The mass-loss rates derived from method 2 are plotted in full line in Fig. 9.

4.3.3. Method 3: from [Fe II] luminosity, emission from shock fronts

The third method to estimate the jet mass-loss rate from the [Fe II] luminosity assumes that the line emission in the elementary aperture is arising from shock fronts. It is described in detail in Hartigan et al. (1995) for the [O I] line. The mass-flux entering the shock, $\dot{M}_s$, is given by

$$\dot{M}_S = \mu m_H n_H V_s A_s,$$

with $\mu = 1.4$, and V_s and A_s, the shock velocity and cross-section respectively.

From the planar atomic J-shock models of Hartigan et al. (2004b), we derive a proportional relation between $n_H V_s$ and the emitted [Fe II] 1.64 μm line flux per shock area (multiplied by 2 to account for both sides of the shock)

$$F_{1.64 \, \mu\text{m}} = 9.69 \times 10^{-14} \times n_H V_s \left(\frac{[\text{Fe/H}]}{[\text{Fe/H}]_\odot}\right) \text{erg s}^{-1} \, \text{cm}^{-2},$$

where we scaled the model fluxes to the recent estimate of solar abundance $[\text{Fe/H}]_\odot = 2.82 \times 10^{-5}$ (Asplund et al. 2005). Integrating over the shock area A_s yields the following equation for the shock mass-flux

$$\dot{M}_S = 9 \times 10^{-8} \, M_\odot \, \text{yr}^{-1} \left(\frac{L_{[\text{FeII}]}}{10^{-4} \, L_\odot}\right) \left(\frac{[\text{Fe/H}]}{[\text{Fe/H}]_\odot}\right)^{-1}. \tag{5}$$

The jet mass flux is related to the mass-flux entering the shock(s) inside the aperture, $\dot{M}_s$, by the following equation (see Hartigan et al. 1995; Cabrit 2002)

$$\dot{M}_J = \dot{M}_s \left(\frac{V_J}{V_s}\right) \left(\frac{\cos \theta}{N_{\text{shock}}}\right), \tag{6}$$

where $\cos(\theta) = A_J/A_s$ for oblique shocks at an angle θ with the flow normal, and N_{shock} is the number of shock fronts within the integration aperture.

Here we assume perpendicular ($\cos \theta = 1$) shock fronts located every 50 AU along the jet (maximum cooling length in the models of Hartigan et al. 2004b). This will tend to give an upper limit to the mass-flux. The [Fe II] luminosity in the HVB and
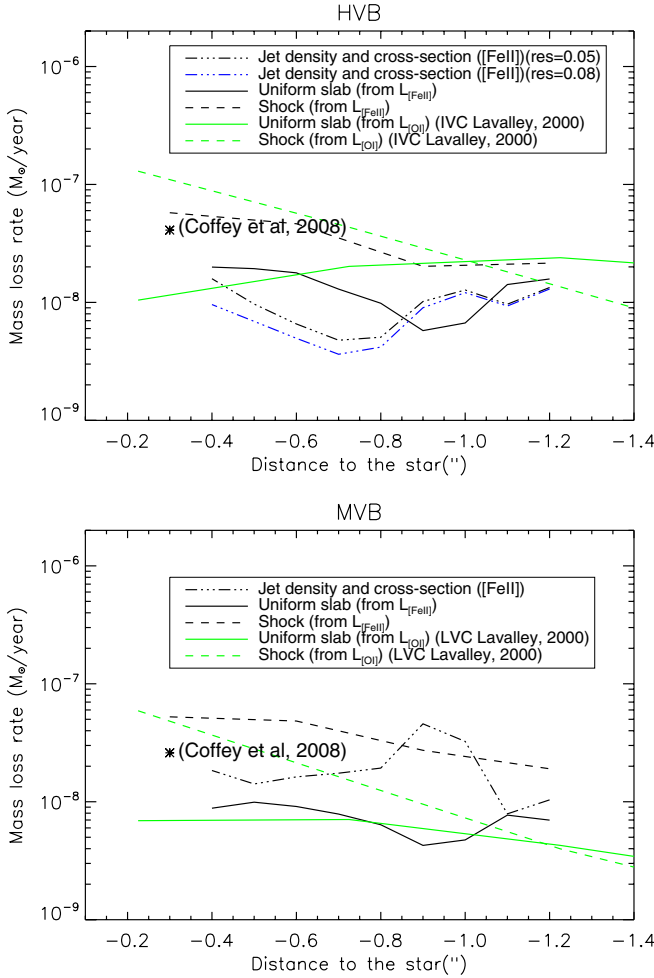
Fig. 9. Values of the mass-loss rate for the atomic blueshifted jet as a function of projected distance to the star and for the two velocity components: HVB (*top panel*) and MVB (*bottom panel*). The values derived from the [Fe II] 1.64 μm observations using the three methods discussed in the text are plotted with black curves: jet density and cross-section (dashed-dotted curve), uniform slab (full curve), shock front (dashed curve). The values obtained by Lavalley-Fouquet et al. (2000) using the optical line [O I] and methods 2 and 3 are shown for comparison (gray/green curves). Star symbols show the values obtained by Coffey et al. (2008) from an optical HST/STIS transverse slit at –0''.3.

MVB channel maps is integrated every 0.3'' = 50 AU along the jet axis, so that $N_{\rm shock}$ = 1. In addition, following the estimates of shock velocities derived by Lavalley-Fouquet et al. (2000), we adopted $V_{\rm J}/V_{\rm s}$ = 4 in the HVB and $V_{\rm J}/V_{\rm s}$ = 2 in the MVB intervals. Finally, we corrected for the Fe gas-phase depletion estimated in the previous section in the shock hypothesis, using [Fe/H]/[Fe/H]$_\odot$ = 1/3 and 1/10 for the HVB and MVB respectively. The derived mass-loss rates are represented with a dashed line in Fig. 9.

4.3.4. Comparison of the three methods

We plot in Fig. 9 the mass-loss rate estimates in the blue DG Tau jet as a function of distance to the star obtained for the three methods, with a separate panel for the HVB [–300, –160] km s^{-1} and MVB [–160, –50] km s^{-1} velocity intervals. The three methods agree reasonably well within a factor 2–5 at all distances from the star, lending some confidence to these values, and to our depletion estimates.

For comparison, the mass-fluxes obtained by Lavalley-Fouquet et al. (2000) in their IVB and LVB intervals using the optical line [O I] and methods 2 and 3 are also shown in Fig. 9 (gray/green curves). They were scaled up by 1.44 to be consistent with the new solar oxygen abundance [O/H]$_\odot$ = 4.57 $\times 10^{-4}$ of Asplund et al. (2005). Because the iron depletion was inferred from the [O I] to [Fe II] luminosity ratio assuming the same jet density in the two epochs, it is expected that both lines should give identical mass-fluxes. The slight differences observed stem from the use of slightly different velocity intervals (IVB, LVB rather than HVB, MVB), and from the fact that the [O I] luminosity is not strictly proportional to $n_{\rm H}V_{\rm s}$ in shocks (the slope is steeper than 1), so that method 3 is less accurate for [O I] than for [Fe II].

Averaging our [Fe II] mass-flux estimates over the central 1'' gives a mass-loss rate of $1.7\pm0.7\times10^{-8}$ $M_\odot$ yr^{-1} for the HVB and $1.6 \pm 0.9 \times 10^{-8}$ $M_\odot$ yr^{-1} for the MVB using the three methods (the quoted uncertainty range is the 1-sigma dispersion about the mean). Our derived HVB mass-loss rate is consistent with the lower limit of 1.2×10^{-8} $M_\odot$ yr^{-1} estimated by Beck et al. (2010) from high-velocity extended HI Brγ emission. The total mass-loss rate for the [Fe II] emitting atomic gas in the velocity range –300 to –50 km s^{-1} is therefore $\dot{M}_{\rm J} \simeq 3.3 \pm 1.1 \times 10^{-8}$ $M_\odot$ yr^{-1}, with approximately equal contribution from the HVB and the MVB. This value is a lower limit to the total mass-loss rate of the atomic component because the [Fe II] emission does not probe the whole range of velocities seen at optical wavelengths.

4.4. Accretion rate and ejection-to-accretion ratio in DG Tau

Muzerolle et al. (1998) have shown that the luminosity of the Brγ line in a large sample of T Tauri stars is well correlated with the accretion luminosity onto the star inferred from modeling of the optical-UV excess. During our SINFONI run, we also obtained K-band data including the Brγ line. We find that any spatially Brγ extended component contributes at most 2% of the total line flux integrated over all velocities. This is consistent with the recent finding of Beck et al. (2010), who show that although extended high-velocity Brγ emission is detected along the DG Tau blueshifted jet, the extended component makes up 2% of the total (velocity integrated) line flux. We therefore make the assumption below that all the HI Brγ flux in DG Tau is related to the accretion process. From our flux-calibrated data we derived a K-band continuum of 7.1 mag and a Brγ equivalent width of 5.6 Å corresponding to a line brightness of 3.9×10^{-16} W m^{-2} and line luminosity of 2.5×10^{-4} $L_\odot$ after extinction correction by $A_{\rm V}$ = 1.6 mag (Gullbring et al. 2000). Using the empirical fit of Muzerolle et al. (1998), we derived an accretion luminosity $L_{\rm acc}$ = 0.77 $L_\odot$ for DG Tau in October 2005. Assuming that the luminosity arises from an accretion shock at the base of an accretion column anchored at the inner disk truncation radius R_i, the mass accretion rate onto the star is then obtained from (Gullbring et al. 1998)

$$\dot{M}_{\rm acc} = \frac{L_{\rm acc}R_\star}{GM_\star}\left(1 - \frac{R_\star}{R_i}\right)^{-1}. \tag{7}$$

Taking $R_i \simeq 5$ $R_\star$ as in Gullbring et al. (1998), and adopting for DG Tau a stellar radius of $R_\star$ = 2.3 $R_\odot$ and a stellar mass of $M_\star$ = 0.7 $M_\odot$ (Hartigan et al. 1995) we derived an accretion rate of $\dot{M}_{\rm acc}$ = 10^{-7} $M_\odot$ yr^{-1}. With a similar Brγ flux (4.5×10^{-16} W m^{-2}), Beck et al. (2010) derive $\dot{M}_{\rm acc}$ = 9.6×10^{-8} $M_\odot$ yr^{-1} using $A_{\rm V}$ = 3.3 mag and a stellar mass of 2.2 $M_\odot$ for DG Tau from White & Hillenbrand (2004). We

note that this value of $\dot{M}_{\rm acc}$ only probes the *instantaneous* accretion rate from the inner disk onto the stellar surface in October 2005. It is not necessarily representative of the mean accretion level pertaining to the period 2002−2004 when the jet material probed by our SINFONI observations was ejected (see Fig. 7).

Indeed, diagnostics of the accretion shock, such as the Brγ and Ca II line strength or the optical veiling, are known to be highly variable in T Tauri stars on scales from days to years, especially in stars as active as DG Tau. Muzerolle et al. (1998) measured in 1998 a Brγ equivalent width 3 times larger than ours, $EW(\mathrm{Br}\gamma) = 14.1$ Å, and obtained a 3 times higher accretion rate, assuming a typical K-band magnitude for DG Tau $K = 6.74$ (average of 17 measurements, provided in Kenyon & Hartmann 1995). Gullbring et al. (2000) derived $\dot{M}_{\rm acc} = 5 \times 10^{-7}\ M_\odot\ {\rm yr}^{-1}$, by fitting an accretion shock model to the Balmer and UV excess continuum emission measured in 1996. Finally, the mean correlation between CaII line luminosity and accretion rate in T Tauri stars suggests $\dot{M}_{\rm acc} \simeq 2 \times 10^{-7}\ M_\odot\ {\rm yr}^{-1}$ in DG Tau in 2002−2003 (Mohanty et al. 2005).

Below we therefore adopt $\dot{M}_{\rm acc} = (3 \pm 2) \times 10^{-7}\ M_\odot\ {\rm yr}^{-1}$ as the possible range of accretion rate prevailing in DG Tau. This is significantly lower than the $\dot{M}_{\rm acc} = 2 \times 10^{-6}\ M_\odot\ {\rm yr}^{-1}$ obtained by Hartigan et al. (1995) from an analysis of the optical veiling in 1988−1989. However, the method of HEG95 systematically tends to overestimate accretion rates in T Tauri stars by an order of magnitude on average (Gullbring et al. 1998).

From the range of mass-flux rates derived in the [Fe ɪɪ] jet (see Sect. 4.3), we thus inferred for the blueshifted jet lobe a ratio of ejection to accretion rates of 0.04−0.4 for the [Fe ɪɪ] emitting flow, with about equal contributions from the MVB and HVB ranges. Most of the uncertainty in this ratio (a factor 5) arises from the mass-accretion rate. The ratio is substantially higher than previously reported by Lavalley-Fouquet et al. (2000), mainly because they adopted a 10 times higher accretion rate from Hartigan et al. (1995). It is compatible with the average ejection to accretion ratio for one jet lobe of ≃0.1 in atomic T Tauri jets obtained by Cabrit (2007b) when comparing [O ɪ] mass-flux rates from spatially unresolved data (Hartigan et al. 1995) with revised mass-accretion rates from Gullbring et al. (1998). Our mass-flux estimates therefore do not appear to suffer from a strong systematic bias.

4.5. Implications for jet launching models

Our results on mass-fluxes, kinematics, and iron depletion in the DG Tau jet have several implications for proposed jet origins.

First, we note that the observed velocities in excess of -50 km s^{-1} in the blueshifted [Fe ɪɪ] flow are much too high to be produced by disk photo-evaporation. Indeed, in photo-evaporated flows terminal velocities reach at most $3-4 \times$ the sound speed $c_{\rm S}$ at the base of the flow (Font et al. 2004). Maximum temperatures of ≃10^4 K reached at the inner disk surface through EUV and X-ray irradiation (Ercolano et al. 2009; Gorti & Hollenbach 2009) would thus lead to terminal velocities $\leq 30-40$ km s^{-1}, much lower than observed in [Fe ɪɪ].

One might wonder if the MVB flow could trace matter entrained and accelerated in a mixing layer between the high-velocity jet (traced by the HVB) and the outer photo-evaporated disk wind. The most recent computations of disk photo-evaporation (Owen et al. 2010; Gorti & Hollenbach 2009), including X-ray irradiation, indeed predict mass-flux rates that could reach $10^{-9}-10^{-8}\ M_\odot\ {\rm yr}^{-1}$ over the entire disk, sufficient to supply the MVB flux. However, the same models

show that most of the photoevaporated mass-flux arises from disk radii $r \geq 5$ AU (Gorti & Hollenbach 2009; Owen et al. 2010). The corresponding streamlines (see Owen et al. 2010, Fig. 3) have cylindrical radii >20 AU for altitudes above the disk $z > 30$ AU, significantly wider than the derived HVB jet radius (see Fig. 3); therefore, one expects very little or no entrainment of the photoevaporated flow by the HVB jet.

Second, we note that the gas-phase depletion of iron, if confirmed, rules out an origin in the stellar surface, at least for the [Fe ɪɪ] MVB emitting material. Indeed, recent determination of photospheric [Fe/H] for young stars in Taurus are compatible with solar abundance (Santos et al. 2008; D'Orazi et al. 2011). Lower [Fe/H] ratios (≃0.2 solar) have been derived in X-rays tracing coronal material but in these observations the [Fe/O] abundance ratio is 0.4−0.8 solar (Scelsi et al. 2007; Günther et al. 2007). These abundance patterns cannot reproduce the low [Fe/O] ratios (≃0.1 solar) inferred in the MVB emitting gas, indicating that the observed Fe gas phase depletion is likely caused by depletion onto dust grains. Our observed Fe depletion pattern also excludes the fact that the medium-velocity conical sheath surrounding the jet could trace a cocoon of matter ejected sideways from the narrow high-velocity beam. Sideways ejected material should be *equally or less* depleted onto dust (more shock-processed) than the faster central beam, whereas we observe the opposite, with a 3 times larger depletion at lower velocity (see Sect. 4.2). It is difficult to pinpoint more precisely the launch radius from the depletion alone; the dust sublimation radius in DG Tau appears to be $r_{\rm sub} \simeq 0.14$ AU from K-band interferometric measurements (Akeson et al. 2005). However, the K-band size may be only an upper limit to $r_{\rm sub}$ owing to the effect of scattered light (Pinte et al. 2008). Ejection from near corotation ($r_{\rm corot} = 0.06$ AU in DG Tau with a stellar period of 6.2 days and assuming a 0.7 $M_\odot$ star) is thus not totally excluded at this stage, pending more detailed models. Ejection from slightly beyond 0.1 AU is not ruled out either, because sublimation starts further out for smaller grains, and only 10−33% of the dust appears to have been destroyed in the [Fe ɪɪ] jet. In addition, $r_{\rm sub}$ could be larger than the K-band radius if the inner disk of DG Tau is optically thick in the gas continuum.

Below, we confront the DG Tau jet properties with predictions for proposed ejection processes, including the X-wind model and an extended MHD disk-wind model.

4.5.1. The X-wind model

The X-wind model assumes that the disk is not intrinsically magnetized and is threaded only by the stellar dipole. It posits that stellar fieldlines are bunched up at the corotation radius and are partly opened in a fan-like configuration along which a centrifugal wind, carrying off the angular momentum from the funnel flow, is assumed to be launched. The semi-analytical wind solution is characterized by an axial density enhancement (the jet) surrounded by a wide-angle flow, where the speed is nearly constant across all streamlines (Shang et al. 1998). This predicted constant flow speed stems from the cylindrical shape of the Alfvén surface, which appears to be a generic property of the X-wind (Cai et al. 2008). Because all streamlines are launched from the same radius $r_0 = r_{\rm corot}$, their magnetic lever arm parameter $\lambda = (r_A/r_0)^2$ is also the same, and so is the terminal speed after magneto-centrifugal acceleration (Blandford & Payne 1982)

$$V_p^\infty = \sqrt{2\lambda - 3}\, V_{\rm Kep}(r_0). \qquad (8)$$

The steep velocity decrease across the DG Tau blueshifted jet seen in Figs. 4 and 5, from $V = -200$ km s^{-1} in the HVB for angles to the jet axis less than 4° to $V = -100$ km s^{-1} in the MVB for angles to the jet axis of 14° and down to -30, -40 km s^{-1} at wider angles in [O I] and [S II] (Bacciotti 2002; Coffey et al. 2007), is clearly not compatible with this characteristic property. The X-wind model could account for the [Fe II] HVB component only, but this would require that the MVB flow originates in an MHD disk wind (because it cannot be explained by photo-evaporation, see above). However, as discussed in Ferreira et al. (2006), it is very unlikely that an X-wind and an extended MHD disk-wind will coexist because this would imply a hole in the disk magnetic flux distribution between these two components. Therefore the X-wind model as currently envisioned does not explain the kinematics in the [Fe II] DG Tau jet.

4.5.2. Conical wind from the disk-magnetosphere boundary

Recent numerical simulations of the interaction between a stellar dipole and a disk with no net magnetic field yield a situation somewhat different from the (semi-analytical) X-wind model (Romanova et al. 2009). As the stellar fieldlines are bunched up by accretion and stretched, a narrow conical wind is formed along the neutral line (rather than in the angular sector below it), and powered by the magnetic pressure force (rather than by the centrifugal force as in the X-wind). In the standard (non-propeller) regime relevant to DG Tau, where the star rotates slowly, the total mass-flux rate in the conical wind is about $10-30\%$ of the accretion rate onto the star, compatible with the observational constraint. A strong transverse velocity gradient is also present, with faster matter from the stellar magnetosphere on the inside and slow matter from the disk on the outside. However, most of the wind mass reaches a low poloidal speed of about 40 km s^{-1} for the CTTS dimensional scalings appropriate in DG Tau: $v_p \simeq 0.2v_0$ with $v_0 = 197$ km s^{-1} in Table 1 of Romanova et al. (2009). And the half-opening angle of 30°−40° is much wider than the 4−15° observed in [Fe II]. Therefore the conical wind as modeled in this work appears both too slow and too broad to explain the [Fe II] jet observations, although it could match the LV sheath surrounding the jet observed in optical lines (Bacciotti 2002). In this framework, the whole [Fe II] jet (HVB and MVB) would have to originate mainly in the stellar surface. This would contradict with the observed iron gas-phase depletion in the DG Tau jet, indicative of a substantial dust content.

4.5.3. Extended MHD disk wind

Protostellar disks may indeed harbor a substantial magnetic flux, advected during the initial infall phase of star formation. If the field is slightly below equipartition, rotation remains quasi-Keplerian in the disk midplane and angular momentum can be efficiently extracted by magnetic torques to launch a powerful wind from the disk surface, as shown by analytical and numerical 2D solutions of the vertical disk structure (Ferreira 1997; Zanni et al. 2007). Pesenti et al. (2004) found that a self-similar, steady MHD wind from a warm disk (Casse & Ferreira 2000), with a lever arm parameter $\lambda = (r_A/r_0)^2 \simeq 13$ could fit the tentative jet rotation signatures observed in the low-velocity [O I] flow (Bacciotti 2002). The same type of model can also reproduce observed jet widths in T Tauri stars (Ray et al. 2007). We now check whether this model could also explain the speed, mass-flux, and depletion in each of the [Fe II] velocity components.

We may use the range of flow speeds in each [Fe II] velocity component to constrain the range of ejection radii in the considered disk wind model. The asymptotic velocity given in Eq. (8) is reached only far from the star in self-similar solutions (Ferreira et al. 2006). We therefore use here the exact predicted flow speeds at an altitude of 50 AU above the disk for the $\lambda = 13$ model, plotted as a thick black curve in Fig. 3 of Ferreira et al. (2006) (note that velocities in that graph are scaled by $1/\sqrt{M_\star/M_\odot}$). The radial velocity range of 160 to 250 km s^{-1} for the HVB component (Pyo et al. 2003) corresponds to deprojected flow speeds of 210–350 km s^{-1} and to launch radii of 0.08 AU to 0.25 AU for a stellar mass $M_\star = 0.7\ M_\odot$. The upper value is consistent with the outer launch radius of $0.2-0.5$ AU for the HVB gas derived from tentative rotation signatures in optical/near-UV lines (Coffey et al. 2007). Similarly, the radial velocity range of $[-50, -160]$ km s^{-1} of the MVB, and deprojected speeds of $70-210$ km s^{-1}, would imply launch radii of $0.25-1.5$ AU. The observed Fe depletions could be explained if 10% of dust is already destroyed around 1 AU and 33% around 0.2 AU. Detailed modeling including a dust size distribution and opacity of the gas disk are needed to see whether this is compatible with K-band size measurements (Akeson et al. 2005).

The ejection-to-accretion ratio for one jet lobe in a self-similar MHD disk wind powered by angular momentum extraction from the disk is given by (Ferreira et al. 2006)

$$\frac{\dot{M}_J}{\dot{M}_{acc}} = \frac{1}{4(\lambda - 1)} \log(r_e/r_i) = \frac{1}{2(\lambda - 1)} \log(V_{max}/V_{min}), \qquad (9)$$

where r_e and r_i are the external and internal radii of the wind launch zone, and V_{min} and V_{max} the corresponding minimum and maximum flow speeds. With $\lambda = 13$, and values of V_{min} and V_{max} as above, one expects an ejection/accretion ratio for one jet lobe of 0.04 in the MVB and 0.02 in the HVB intervals, respectively. This is compatible within uncertainties with the mass-fluxes estimated here (see Sect. 4.3) if the DG Tau accretion rate during the period (2002−2004) was $\simeq 5 \times 10^{-7}\ M_\odot$ yr^{-1}, near the upper end of the range reported in recent works (see Sect. 4.4). Clearly, a closer monitoring of accretion and ejection signatures in DG Tau over a few years is required to estimate more accurately the ejection/accretion ratio in the DG Tau jet, and provide a more definitive test.

We stress that the above comparison must be taken as indicative only. First, we have discussed the implications in the context of a specific disk wind solution with $\lambda = 13$. A smaller λ solution may be more compatible with the mass flux constraints. A thorough investigation of possible disk wind solutions compatible with all observational constraints should be conducted. Secondly, the above comparison assumes that the periodic knots/bubbles do not significantly modify the overall steady-state disk wind kinematics and mass-flux (even though they will locally modify its *ionization level* through shocks). The period of knot generation of 2.5 years in DG Tau is about 140 times the star rotation period of 6.2 days, i.e. much longer than the orbital timescale in the inner disk, but comparable to the orbital period at 1.5 AU. Therefore, the steady-state disk wind assumption could be valid for the HVB, but only marginal for the MVB flow. The formation of large bubbles in the wake of knots may further perturb the structure of the outer disk wind.

Large-scale flares over similar long timescales, followed by a re-arrangement of outflow density and velocity distribution, were recently observed in long-term numerical simulations of an extended disk wind interacting with the stellar magnetosphere (Fendt 2009). This scenario could be promising to explain the

DG Tau jet properties, although simulations over larger spatial scales would be needed to compare with our observations. Alternatively, a stellar magnetic cycle could be at the origin of the time variability observed in the launching process or the period of 2.5 years might correspond to an excentric binary companion perturbing the inner disk at periastron passage. Studies of jet wiggling and interferometric imaging of DG Tau could help in testing this last alternative.

4.5.4. Episodic magnetic bubbles

Based on recent laboratory experiments of radiatively cooled plasma jets, Ciardi et al. (2009) propose yet another possible ejection mechanism for the DG Tau jet. Starting from a highly wound-up field configuration with $|B_\phi| \propto r^{-1} \gg B_p$ and a strong axial current, two outflow components are generated: a magnetic bubble (or cavity) accelerated by gradients of the magnetic pressure and surrounded by a shell of swept-up ambient material, and a magnetically confined narrow jet on the bubble axis. This process is akin to the magnetic tower modeled numerically e.g. by Kato et al. (2004), although it is followed over longer timescales and with higher resolution. Repetitive outflow cavities are produced as the plasma refills in the launch region. The new cavities are confined by the matter left over from previous episodes, so that collimation properties gradually become independent of initial conditions. The morphology is suggestive of that of DG Tau, with a collimation angle of $\leq 10°$ for the high-density clumps along the axis. However, the bubbles already inflate very close to the disk so that the conical geometry of the MVB flow is not well reproduced. Additional confinement of the bubbles by a surrounding disk wind may be required to explain this property. Further work in this direction would be extremely valuable, as would numerical estimates of the required $|B_\phi|$ in the DG Tau disk.

5. Conclusions

- We observed an onion-like kinematic structure in the blueshifted jet with a conical medium-velocity (MVB) flow at $V \simeq -100$ km s^{-1} surrounding a more tightly collimated high-velocity (HVB) beam at $V \simeq -200$ km s^{-1}. The velocity fluctuations and electronic density distribution along the jet show little variation between 1998 and 2005. However, little [Fe II] emission is observed from the low-velocity (LV) flow component at $\simeq -30, -40$ km s^{-1} reported in optical lines at 30 AU from the jet axis.

- By comparing the intensities in [Fe II] and [O I] in the DG Tau jet at two epochs, we infer evidence for iron depletion by a factor 10 at speeds below 100 km s^{-1}, and by a factor 3 in the high-velocity range. Simultaneous data are required to confirm this result. Mass-flux rates for the blueshifted jet lobe inferred from three independent methods are $1.6 \pm 0.8 \times 10^{-8}$ $M_\odot$ yr^{-1} in each of the MVB and HVB ranges, representing 0.02–0.2 of the disk accretion rate each.

- The counterjet is dominated by a striking bubble structure. A similar faint bubble structure is also detected in the blueshifted lobe. The radial and tangential velocity in the red lobe is lower than in the blue lobe by a factor $\simeq 0.7$. The observed central obscuration, if caused by extinction by the disk, favors the similarity solution for the DG Tau disk surface density distributions derived by Isella et al. (2010) rather than a sharply truncated power law.

- The two new knots present in the blueshifted lobe indicate the presence of a variability timescale of 2.5 years over the last 10 years, two times shorter than estimated by Pyo et al. (2003), and 140 times longer than the stellar rotation period. The current bubble structures appear to have formed in the wake of the high-velocity knot observed by Pyo et al. (2003), ejected in 1999. Observations more closely spaced in time would help to clarify the knot/bubble dynamics and the origin of these quasi periodic eruptions. Searches for periodic changes in mass accretion rate and for jet wiggling would also constrain the process responsible for these transient events.

- The velocities of the [Fe II] MVB flow are too high to be accounted for by disk photo-evaporation models. Origin of the MVB component in entrainment of an outer photo-evaporated disk wind seems also unlikely owing to the derived narrow HVB jet widths. The strong iron depletion also rules out an origin in a stellar wind, or in sideways ejected matter from the (3 times less depleted) HVB beam. In addition, neither the classical X-wind model (Shang et al. 1998; Cai et al. 2008) nor the conical wind found in recent simulations of stellar magnetosphere-disk interaction (Romanova et al. 2009) are able to reproduce the kinematics and opening angles in the [Fe II] MVB. A dusty MHD disk wind appears to be the most plausible origin for this component.

- The extended MHD disk-wind solution proposed to fit optical rotation signatures in DG Tau (Pesenti et al. 2004) compares more favorably with observations. It predicts launch radii of 0.08–0.25 AU and 0.25–1.5 AU, respectively, for the HVB and MVB velocity ranges, consistent with the higher iron depletion at lower speed. The predicted mass-fluxes also agree with observed values if the accretion rate was relatively high in DG Tau over 2002–2004, $\simeq 5 \times 10^{-7}$ $M_\odot$ yr^{-1}. However, contribution from magnetospheric reconnexions or magnetic towers may not be negligible, modifying the predicted flow structure. Spectro-imaging monitoring of accretion and ejection signatures in DG Tau over a few years are essential to elucidate the ejection processes at work in this prototypical source.

References

Agra-Amboage, V., Dougados, C., Cabrit, S., Garcia, P. J. V., & Ferruit, P. 2009, A&A, 493, 1029
Akeson, R. L., Boden, A. F., Monnier, J. D., et al. 2005, ApJ, 635, 1173
Anderson, J. M., Li, Z.-Y., Krasnopolsky, R., & Blandford, R. D. 2003, ApJ, 590, L107
Asplund, M., Grevesse, N., & Sauval, A. J. 2005, in Cosmic Abundances as Records of Stellar Evolution and Nucleosynthesis, ed. T. G. Barnes, III, & F. N. Bash, ASP Conf. Ser., 336, 25
Bacciotti, F. 2002, in Rev. Mex. Astron. Astrofis. Conf. Ser. 13, ed. W. J. Henney, W. Steffen, L. Binette, & A. Raga, 8
Bacciotti, F., & Eislöffel, J. 1999, A&A, 342, 717
Bacciotti, F., Mundt, R., Ray, T. P., et al. 2000, ApJ, 537, L49
Beck, T. L., Bary, J. S., & McGregor, P. J. 2010, ApJ, 722, 1360
Beck-Winchatz, B., Bohm, K.-H., & Noriega-Crespo, A. 1996, AJ, 111, 346

Blandford, R. D., & Payne, D. G. 1982, MNRAS, 199, 883
Bonnet, H., Conzelmann, R., Delabre, B., et al. 2004, in SPIE Conf. Ser. 5490, ed. D. Bonaccini Calia, B. L. Ellerbroek, & R. Ragazzoni, 130
Cabrit, S. 2002, in EAS Pub. Ser. 3, ed. J. Bouvier, & J.-P. Zahn, 147
Cabrit, S. 2007a, in Lect. Notes Phys. (Berlin: Springer Verlag), 723, 21
Cabrit, S. 2007b, in IAU Symp. 243, ed. J. Bouvier, & I. Appenzeller, 203
Cai, M. J., Shang, H., Lin, H., & Shu, F. H. 2008, ApJ, 672, 489
Casse, F., & Ferreira, J. 2000, A&A, 361, 1178
Cerqueira, A. H., Velázquez, P. F., Raga, A. C., Vasconcelos, M. J., & de Colle, F. 2006, A&A, 448, 231
Ciardi, A., Lebedev, S. V., Frank, A., et al. 2009, ApJ, 691, L147
Coffey, D., Bacciotti, F., Ray, T. P., Eislöffel, J., & Woitas, J. 2007, ApJ, 663, 350
Coffey, D., Bacciotti, F., & Podio, L. 2008, ApJ, 689, 1112
Combet, C., & Ferreira, J. 2008, A&A, 479, 481
D'Orazi, V., Biazzo, K., & Randich, S. 2011, A&A, 526, 103
Dougados, C., Cabrit, S., Lavalley, C., & Ménard, F. 2000, A&A, 357, L61
Edwards, S. 2009, in AIP Conf. Ser., ed. E. Stempels, 1094, 29
Eisenhauer, F., Abuter, R., Bickert, K., et al. 2003, in SPIE Conf. Ser. 4841, ed. M. Iye, & A. F. M. Moorwood, 1548
Ercolano, B., Clarke, C. J., & Drake, J. J. 2009, ApJ, 699, 1639
Fendt, C. 2009, ApJ, 692, 346
Ferreira, J. 1997, A&A, 319, 340
Ferreira, J., Dougados, C., & Cabrit, S. 2006, A&A, 453, 785
Font, A. S., McCarthy, I. G., Johnstone, D., & Ballantyne, D. R. 2004, ApJ, 607, 890
Gorti, U., & Hollenbach, D. 2009, ApJ, 690, 1539
Gullbring, E., Hartmann, L., Briceno, C., & Calvet, N. 1998, ApJ, 492, 323
Gullbring, E., Calvet, N., Muzerolle, J., & Hartmann, L. 2000, ApJ, 544, 927
Günther, H. M., Schmitt, J. H. M. M., Robrade, J., & Liefke, C. 2007, A&A, 466, 1111
Hartigan, P., Edwards, S., & Ghandour, L. 1995, ApJ, 452, 736
Hartigan, P., Edwards, S., & Pierson, R. 2004a, ApJ, 609, 261
Hartigan, P., Raymond, J., & Pierson, R. 2004b, ApJ, 614, L69
Isella, A., Carpenter, J. M., & Sargent, A. I. 2010, ApJ, 714, 1746
Kato, Y., Hayashi, M. R., & Matsumoto, R. 2004, ApJ, 600, 338
Kenyon, S. J., & Hartmann, L. 1995, ApJS, 101, 117
Kwan, J., Edwards, S., & Fischer, W. 2007, ApJ, 657, 897

Lavalley, C. 2000, Ph.D. Thesis, Université Joseph Fourier, Grenoble 1
Lavalley, C., Cabrit, S., Dougados, C., Ferruit, P., & Bacon, R. 1997, A&A, 327, 671
Lavalley-Fouquet, C., Cabrit, S., & Dougados, C. 2000, A&A, 356, L41
Mohanty, S., Jayawardhana, R., & Basri, G. 2005, ApJ, 626, 498
Mouri, H., & Taniguchi, Y. 2000, ApJ, 534, L63
Mundt, R., & Fried, J. W. 1983, ApJ, 274, L83
Muzerolle, J., Hartmann, L., & Calvet, N. 1998, AJ, 116, 2965
Nisini, B., Caratti o Garatti, A., Giannini, T., & Lorenzetti, D. 2002, A&A, 393, 1035
Nisini, B., Bacciotti, F., Giannini, T., et al. 2005, A&A, 441, 159
Owen, J. E., Ercolano, B., Clarke, C. J., & Alexander, R. D. 2010, MNRAS, 401, 1415
Pesenti, N., Dougados, C., Cabrit, S., et al. 2003, A&A, 410, 155
Pesenti, N., Dougados, C., Cabrit, S., et al. 2004, A&A, 416, L9
Pinte, C., Ménard, F., Berger, J. P., Benisty, M., & Malbet, F. 2008, ApJ, 673, L63
Podio, L., Bacciotti, F., Nisini, B., et al. 2006, A&A, 456, 189
Podio, L., Medves, S., Bacciotti, F., Eislöffel, J., & Ray, T. 2009, A&A, 506, 779
Pradhan, A. K., & Zhang, H. L. 1993, ApJ, 409, L77
Pyo, T.-S., Kobayashi, N., Hayashi, M., et al. 2003, ApJ, 590, 340
Ray, T., Dougados, C., Bacciotti, F., Eislöffel, J., & Chrysostomou, A. 2007, in Protostars and Planets V, ed. B. Reipurth, D. Jewitt, & K. Keil, 231
Romanova, M. M., Ustyugova, G. V., Koldoba, A. V., & Lovelace, R. V. E. 2009, MNRAS, 399, 1802
Santos, N. C., Melo, C., James, D. J., et al. 2008, A&A, 480, 889
Scelsi, L., Maggio, A., Micela, G., Briggs, K., & Güdel, M. 2007, A&A, 473, 589
Shang, H., Shu, F. H., & Glassgold, A. E. 1998, ApJ, 493, L91
Soker, N. 2005, A&A, 435, 125
Terquem, C. E. J. M. L. J. 2003, MNRAS, 341, 1157
Testi, L., Bacciotti, F., Sargent, A. I., Ray, T. P., & Eislöffel, J. 2002, A&A, 394, L31
White, R. J., & Hillenbrand, L. A. 2004, ApJ, 616, 998
Woitas, J., Ray, T. P., Bacciotti, F., Davis, C. J., & Eislöffel, J. 2002, ApJ, 580, 336
Zanni, C., Ferrari, A., Rosner, R., Bodo, G., & Massaglia, S. 2007, A&A, 469, 811